

Composition and mineralogy of dark material units on Vesta



Ernesto Palomba^{a,*}, Andrea Longobardo^a, Maria Cristina De Sanctis^a, Francesca Zambon^a, Federico Tosi^a, Eleonora Ammannito^{a,b}, Fabrizio Capaccioni^a, Alessandro Frigeri^a, Maria Teresa Capria^a, Edward A. Cloutis^c, Ralf Jaumann^d, Jean-Philippe Combe^e, Carol A. Raymond^f, Christopher T. Russell^b

^a INAF, Istituto di Astrofisica e Planetologia Spaziali, via Fosso del Cavaliere, 00133 Rome, Italy

^b UCLA, Los Angeles 90095, USA

^c University of Winnipeg, Canada

^d DLR, Berlin, Germany

^e Bear Fight Institute, 22 Fiddlers Rd., Winthrop, WA 98862, USA

^f Cal. Inst. Tech., Jet Prop. Lab., Pasadena, CA 91125, USA

ARTICLE INFO

Article history:

Received 11 November 2013

Revised 8 March 2014

Accepted 23 April 2014

Available online 2 May 2014

Keywords:

Asteroid Vesta
Spectroscopy
Asteroids, surfaces
Mineralogy
Regoliths

ABSTRACT

Vesta is the asteroid with the largest albedo variation among the known rocky Solar System objects and shows a widespread occurrence of dark material (DM) and bright material (BM) units. In the first observation phases by the Dawn spacecraft, two main extensions of low albedo areas were identified on Vesta and found to be closely correlated with carbonaceous, OH-rich, material. In this work we use the hyperspectral data provided by the VIR-Dawn imaging spectrometer onboard Dawn to detect and analyze individual, well-defined, dark material units. We define DM units assuming a relative criterion, i.e. reflectance lower than the surroundings. By coupling visible and infrared images of the same area we are able to select real dark material units, discarding false detections created by shadowing effects. A detailed final catalogue of 123 dark units is presented, containing the geographical parameters and the main spectral characteristics for each unit. Independently of the geological context of the dark units, all DMs show similar spectral properties, dominated by the pyroxene absorption features, as is the average spectrum of Vesta. This finding suggests a similar composition, with the presence of darkening agents that also weaken pyroxene band depths. The majority (90%) of the DM units shows a positive correlation between low albedo and an OH band centered at 2.8 μm , confirming the hypothesis that the darkening agents are carbonaceous chondrites, probably delivered by low-velocity impacts of primitive asteroids. A comparison with laboratory spectra allows us to better constrain the size and the composition of the darkening agents. These DM areas seem to be made of eucritic material. The regolith grain size seems to be nearly constant around an average value of 25 μm , and is quite homogenous at least in the first hundreds of meters beneath the Vesta surface, suggesting similar processing mechanisms for both DM and BM.

© 2014 Published by Elsevier Inc.

1. Introduction

Prior to 2011, our knowledge of Vesta was derived from space-based and ground-based telescopic observations: visible and near-IR spectroscopy have shown that the surface of Vesta exhibits absorption features indicative of basaltic minerals, similar in composition to the howardite–eucrite–diogenite (HED) family of basaltic achondrite meteorites, leading to the conclusion that Vesta was the most plausible candidate to represent the HED parent body (e.g., McCord et al., 1970; Gaffey, 1997; Binzel et al., 1997).

Ground-based and Hubble Space Telescope (HST) images of Vesta have revealed that the surface is not covered with uniform material, but instead exhibits local color and albedo variations of 10–20% (e.g. Gaffey, 1997; Binzel et al., 1997; Li et al., 2010).

In July 2011 NASA's Dawn spacecraft entered into orbit around Vesta for a year-long mapping phase (Russell et al., 2007, 2012) during which the real nature of the asteroid was unveiled, making remarkable discoveries that strongly improved understanding of the origin and evolution of the Solar System and its building blocks (Russell et al., 2012; De Sanctis et al., 2012a; Jaumann et al., 2012; Prettyman et al., 2012).

During the first year of orbit around Vesta, the Dawn spacecraft took color and hyperspectral images of Vesta by means of the Framing Camera (Sierks et al., 2011) and the Visual and InfraRed

* Corresponding author. Fax: +39 0649934384.

E-mail address: ernesto.palomba@iaps.inaf.it (E. Palomba).

spectrometer (VIR) (De Sanctis et al., 2011) and mapped the surface elemental composition at regional spatial scales by means of the Gamma Ray and Neutron Detector (GRaND) (Prettyman et al., 2011).

Dawn confirmed that Vesta has a composition spanning from the eucritic to the diogenitic, and found a strong dichotomy between the southern and northern hemispheres and between eastern and western hemispheres (Ammannito et al., 2013a; De Sanctis et al., 2012a; Reddy et al., 2012a).

The VIR spectrometer showed that there are considerable regional and local albedo and compositional variations across the asteroid, and that diogenitic components are concentrated mainly in the southern region, particularly matching the Rheasilvia impact basin (De Sanctis et al., 2012a; Ammannito et al., 2013a; McSween et al., 2013).

Furthermore, it has been observed that Vesta is the asteroid with the largest known albedo variations (Reddy et al., 2012a; Li et al., 2013; Prettyman et al., 2012; Denevi et al., 2012). Surface brightness is not uniform, and bright and dark material units (hereafter tagged as BM and DM units) are observed at local scale (Jaumann et al., 2012; McCord et al., 2012; Palomba et al., 2013; De Sanctis et al., 2013; Zambon et al., 2014). DM units are non-randomly distributed across Vesta's surface and often are associated with specific geo-morphological features (Jaumann et al., 2014). Typically DM units are associated with impact features and likely consist of ejecta materials, both inside and outside craters. However, they are also associated with soil movements and mass wasting. In addition to DM units, a broad low-albedo region that extends from 90° to 200° longitude and 64°S to 16°N latitude was observed on Vesta (Jaumann et al., 2014). The characteristics of this region are compatible with the presence of a darkening agent finely mixed with the original Vesta regolith. A plausible explanation is that this material was delivered to Vesta by low-albedo (probably carbonaceous) asteroids over time and that subsequent impact gardening created a mixed layer to depths between one and several kilometers (McCord et al., 2012). An alternative hypothesis is that the dark material is delivered by small carbonaceous chondrite (CM type) particles up to at least centimeter size over a limited time span (De Sanctis et al., 2012b). This event may have delivered CM material during the early evolution of Vesta (after differentiation and crust formation), which upon subsequent cratering may have mixed into the regolith. A major impact may also have produced an uneven distribution. The two scenarios can be considered the two endmembers of the continuous flux scenario, discussed in Turrini et al. (2014), according to which both large stochastic events and micrometeoroid flux can have been occurred onto the Vesta surface.

The carbon-rich, low-velocity impactors discussed in all the scenarios would deposit hydrated compounds onto the dark areas on Vesta, which in fact show a weak but well-defined OH spectral feature at 2.8 μm (De Sanctis et al., 2012b; McCord et al., 2012). Combining seven color Framing Camera images of a representative DM unit samples with laboratory data show a close relationship between DM areas. The broad low albedo areas seems to confirm the possibility that DM originated in a low-velocity (<2 km/s) carbonaceous body during the formation of the 400 km diameter Veneneia basin (Reddy et al., 2012b). This scenario seems to be supported by the recent global distribution found by the Framing Camera, in which many DM units are concentrated in the northern parts of the Veneneia impact basin (Jaumann et al., 2014).

A possible alternative and endogenic source for dark material on Vesta is represented by freshly exposed mafic material or impact melt, created or exposed by impacts, both rich in opaque phases and volcanic units (McCord et al., 2012).

The scope of this paper is to identify and map the locations of dark material units on the surface of Vesta using VIR data. Assum-

ing that the dark materials are more concentrated near their source on the surface, we focused on the detection of areas that combine local extrema of low albedo and high surface temperature. This analysis led us to build a taxonomic catalogue of the different types of deposits, to study the general spectral property trends and individual peculiarities of the low-albedo materials, and to consider all the postulated sources for the darkening. The hypotheses of delivery of carbonaceous chondrites, as well as opaques, or impact-shocked materials will be compared in detail.

The possible causes of darkening such as the grain size variation, the presence of carbonaceous chondrites, impact-shocked materials or opaque rich compounds, are discussed in Section 2. In Section 3 we give an overview of the spectral data used and define the spectral parameters suitable to analyze the mineralogy of DM. We present the methodology adopted to detect DM and their classification in Section 4, whereas in Section 5 we discuss the composition and origin of DM, offering endogenic sources as alternatives (or as complementary) to the exogenic carbonaceous sources or other opaque rich materials. Finally, conclusions are given in Section 6.

2. Darkening agents

There are many agents that can darken a Vis–NIR spectrum that can be at the origin of the DM units on Vesta: grain size, carbonaceous chondrite materials, opaques and metals.

2.1. Regolith grain sizes

It is well known that a general decrease in reflectance is observed with increasing grain size (Adams and Filice, 1967; Clark et al., 1992). For example, on Mars, low albedo regions typically consist of coarse-grained (mm size) regolith whereas bright regions are formed by fine-grained (μm size) dust (Ruff and Christensen, 2002). This behavior is also observed in several laboratory spectra of different materials (e.g. Cloutis et al., 2013). Similarly, and especially in pyroxenes, the increase in grain size will deepen both Band I and Band II and result in band saturation which is achieved for $\sim 100 \mu\text{m}$ (Cloutis et al., 2013).

2.2. Carbonaceous rich material

Among common asteroidal materials, carbonaceous chondrites are some of the darkest. Here, the major opaque darkening phases are represented by magnetite and various carbonaceous phases. The carbonaceous phases refer to material that is rich in carbon. It is fine-grained, finely dispersed and intimately associated with phyllosilicates (Mason, 1962; Pearson et al., 2002; Garvie and Buseck, 2004; Kebukawa et al., 2010; Clemett et al., 2010). As a result, in spite of its low overall abundance (a few percent) it is very effective at darkening the reflectance spectra of carbonaceous chondrites (Gaffey, 1976). Decreasing petrologic grade (from 3 to 1) follows a change in the basic mineralogy from anhydrous to hydrous silicates.

Generally, darker carbonaceous chondrite spectra are correlated with bluer spectral slopes: a behavior most consistent with an increasing abundance of fine-grained magnetite and/or insoluble organic material (IOM). There are many examples of carbonaceous chondrite clasts in howardites, typically with abundances up to 5 vol.% (Zolensky et al., 1996), although one sample (PRA 04401) shows an abundance as high as 60 vol.% (Herrin et al., 2011; Cloutis et al., 2013).

2.3. Impact shock processes

Impact shock of mafic silicates can lower albedo and reduce band depth (Gaffey, 1976; Adams et al., 1979). There are two main processes that are responsible for this. Comminution and dispersion of micron-scale nickel iron metal and troilite are common processes in ordinary chondrites (OC) (e.g. Britt and Pieters, 1994) but should be less efficient in HED, in which the original opaque and metal abundance are significantly lower than in OCs. Glass formation is the other process that is more effective as the abundance of plagioclase is larger in HEDs, and plagioclase is more fragile than pyroxene. Impact shocks experiments of plagioclases show a complex behavior of the measured reflectance versus impact shock, with a decrease in reflectance interrupted by a slight increase coinciding with the onset of diaplectic glass formation. Finally as maskelynite is generated at higher pressures, reflectance further decreases. The overall effect is a general reflectance decreasing with the shock pressure with drops of more than 60% with respect to the unshocked sample (Johnson and Horz, 2003).

As an example, the Padvarninkai eucrite is the one of the most heavily shocked eucrite known with most of the plagioclase converted to maskelynite with significant impact melt glass (Hiroi et al., 1995). There are some other HED examples with abundant impact melts or glasses that demonstrate this process: the polymict eucrite LEW85303 with an impact melt matrix, Macibini, a eucritic breccia with a very large clast composed of 50% devitrified glass and 50% silicates (Buchanan et al., 2000), and Jiddat al Harasis (JaH) 626, a polymict eucrite that experienced significant impact shock and melt quenching (Cloutis et al., 2013; Irving, 2012). However, excluding Padvarninkai and Macibini, both LEW85303 and Jiddat al Harasis show high reflectances not compatible with DM units (Reddy et al., 2012c).

2.4. Opaques and metals

The presence of opaque and metal phases in a moderately bright compound such as pyroxene tends to lower the reflectance. By increasing the metal abundance in a mixture, the overall effect is a decrease in reflectance and in both the BDI and BDII (Cloutis et al., 1990). However, the inventory of opaque-rich eucrites is scarce and the abundance of these phases is not larger than 1% (Mayne et al., 2010).

3. Tools and data reduction

The VIR instrument consists of a single optical head, with two channels, the visible (0.2–1 μm , with 1.8 nm resolution) and the infrared (1–5 μm , with 9.5 nm resolution) and produces hyperspectral data with three dimensions, two spatial and one spectral.

Our DM unit survey was applied to the data obtained during all phases of the mission, characterized by different VIR nominal resolution: Approach (700–1300 m/pixel), Survey (altitude ~ 2700 km and resolution ~ 700 m/pixel); High Altitude Mapping Orbit (HAMO – altitude ~ 685 km and resolution ~ 200 m/pixel); Low Altitude Mapping Orbit (LAMO – altitude ~ 200 km and resolution ~ 70 m/pixel) and HAMO2 (similar altitude and resolution of the HAMO phase), the last phase before departure from Vesta.

3.1. Definitions of spectral parameters

Vesta spectra are dominated by two pyroxene absorption bands, commonly referred to as Band I and Band II and respectively centered at about 0.9 μm and 1.9 μm . To study the spectral properties of dark materials and to understand the mineral composition and possibly the physical characteristics of the regolith (i.e.

effective grain size), we introduce in our analyses spectral parameters such as the band center (BC), the band depth (BD) and the band area ratio (BAR). These spectral parameters have been found to be useful for extracting compositional information from mafic silicate-bearing mixture spectra (Cloutis et al., 1986). For example, band centers are commonly used to analyze the pyroxene composition (e.g. Cloutis and Gaffey, 1991) and the HED type (Burbine et al., 2001), band depths are sensitive to the regolith grain size and to the presence of opaque contaminants (Cloutis et al., 2013), the scatterplot BC–BAR is sensitive to olivine abundance in a mixture olivine–pyroxene and is used to distinguish achondritic from the ordinary chondritic materials, while the BCI–BCII is more suitable to identify significant olivine components in HED-type assemblages (e.g. Cloutis et al., 1986; Duffard et al., 2005; Ammannito et al., 2013b).

Band center is defined as the band minimum after the spectral continuum removal, whereas band depth is defined as: $1 - R_b/R_c$ (Clark and Roush, 1984), where R_b and R_c are the reflectance of the band and the spectral continuum at the BC (Gaffey et al., 2002).

Band area is the area enclosed between the spectral curve and the continuum. BAR (defined in Cloutis et al., 1986) is the ratio between Band II area and Band I area.

Another spectral parameter that proves useful to characterize the studied minerals is the Band II half-width half maximum (HWHM), defined as the distance between the wavelength corresponding to the half of the short wavelength shoulder reflectance and the band minimum (Cloutis et al., 2013).

Following an approach similar to Moskovitz et al. (2010), fourth-order polynomial fits have been used to fit the Band I shoulders (between 0.55 and 0.80 μm , and between 1.10 and 1.69 μm respectively) and the Band I and Band II reflectance troughs (between 0.80 and 1.10 μm and between 1.81 and 2.07 μm respectively).

Band I continuum is defined as the straight line starting from the 0.7 μm maximum and tangent to the spectral curve, whereas Band II continuum is the straight line from the maximum between 1.10 and 1.69–2.40 μm . Typically, the 2.40 μm cut is justified by the possible presence of a water band in laboratory samples, which could affect the retrieval of the spectral parameters relative to Band II (Cloutis et al., 1986).

All the spectral parameters have been calculated on spectra given by the polynomials overlapping in order to improve signal-to-noise ratio.

3.2. Photometric influences

Vis–NIR spectra are strongly affected by illumination conditions: radiation interacts differently with regolith particles, depending on the incidence, emission or phase angles, producing different reflectances and spectral shapes and changing spectral parameters.

Usually, this behavior can be reproduced and corrected by applying a good photometric model to the data. Schroder et al. (2013) and Longobardo et al. (2014) demonstrated that FC and VIR data can be photometrically corrected by applying an Akimov parameter-free disk function (Shkuratov et al., 1999; Eq. (29)) and an appropriate phase function. The former should remove any topographic effects (i.e., dependence on incidence and emission angles), whereas the latter corrects the observational geometry. A statistical analysis of VIR spectra allowed us to retrieve a phase function for both high and low resolution data at 0.75 μm and 1.2 μm (Longobardo et al., 2014). These phase functions have been used to obtain a photometrically corrected reflectance at these wavelengths. Also the band depths have been corrected by applying the empirical phase function found by Longobardo et al. (2014).

To properly compare VIR data with laboratory results, reflectance and band depths were calculated at the following conditions: incidence angle 30° , emission angle 0° and phase angle 30° .

In terms of other effects on band centers, laboratory measurements showed that they are influenced by temperature variations (e.g., Burbine et al., 2009; Reddy et al., 2012c). In particular, they move towards longer wavelengths with increasing temperature. This has been observed also in the Vesta dataset, in the limit allowed by the Vestan temperature range. Longobardo et al. (2014) found that the Band I and Band II center displacements are $5.5 \cdot 10^{-5} \mu\text{m K}^{-1}$ and $18 \cdot 10^{-5} \mu\text{m K}^{-1}$, respectively. These band center–temperature slopes have been applied to VIR data in order to retrieve the band center location at a temperature of 300 K, i.e., a temperature where laboratory spectra are usually acquired. On average, the band center shift is comparable or lower than the VIR IR spectral resolution: considering a Vestan average surface temperature of 250 K, the band centers displacement is about 3 nm for the Band I, and about 9 nm for Band II.

Finally, the BAR is not affected by illumination angles, as observed on both HED spectra (Beck et al., 2011) and VIR spectra (Longobardo et al., 2014).

For each of the DM units, the mean value of spectral parameters introduced above have been calculated on the whole dark region in order to emphasize possible correlations between darkening and spectral parameters.

4. Dark material unit catalogue and classification

4.1. DM catalogue definition

Low-albedo regions found on Vesta span very different extents (from 1 to 20 square degrees) with varying degrees of reflectance (from 0.1 to 0.23) among and within some units. Further, shadows and lighting conditions can affect detection and mapping of DM. Although Vesta is one of the largest main belt asteroids, it is small enough so that the interaction of the light with geomorphological structures such as steep slopes or impact features (Jaumann et al., 2012) can be exaggerated, creating play of light and elongated shadows projected on the surface, even in photometrically corrected images. This is due to the fact that the photometric correction takes into account the observation angles averaged over the area intercepted by each pixel. Nevertheless, the incidence and emission angle can strongly vary within this area, and this occurs especially near the crater rims. This generates shadows inside the region intercepted by each pixel, dramatically lowering the corresponding albedo and leading to a false positive detection of a DM unit.

To overcome this complication and obtain a precise discrimination of DM, we adopt a functional definition of DM units, based on two parameters, photometrically-corrected reflectance and tem-

perature. The method followed to retrieve temperatures from VIR infrared data is detailed in the Appendix of Tosi et al. (2014). It is basically a Bayesian approach to nonlinear inversion that already proved to be successful for Rosetta/VIRTIS data of asteroid Lutetia (Coradini et al., 2011; Keihm et al., 2012), and that was extensively applied to the entire VIR data archive obtained at Vesta. Compared to other approaches, the Bayesian approach does not require any extrapolation of the spectral reflectance in the thermal region, allows a simultaneous retrieval of the unknown quantities (temperature and emissivity), and offers a clear way to include an a-priori hypothesis (i.e., the best estimate of the unknown parameters prior to their measure) in the solution.

We do not adopt an “absolute” definition of a dark region, i.e., a region with a reflectance lower than a certain threshold. Instead, we will adopt a *relative* definition of dark unit, i.e., a region darker than the surroundings that allows us to identify the presence of a darkening end-member even in brighter regions. Similarly, a relative definition has been adopted for bright material units (Li et al., submitted for publication).

By combining albedo and thermal emission of a pixel (or a group of pixels) we are able to distinguish shadows from genuine DM units: a shadowed region would appear dark and will be cooler than the surroundings; conversely, a genuine DM unit is warmer or shows similar temperatures than the surrounding lit regions. An example of how this happens for a false positive and a “real” DM detection, is shown in Fig. 1. The DM catalogue was built by dividing the dark material units in two main groups: Very Dark and Dark, depending on their reflectance value at $1.2 \mu\text{m}$ compared to the reflectance average value of the entire image cube.

If $R_{1.2}$ is the albedo as measured by VIR and T is the temperature as obtained by VIR thermal spectra then a Dark Material (DM) or a Very Dark Material (VDM) area is found if $R_{1.2}$ is 15% and 30% lower than the frame average $R_{1.2m}$, respectively. The first threshold, i.e., 15%, is the $1.2 \mu\text{m}$ reflectance difference between a typical dark and a typical intermediate Vestan material (McCord et al., 2012, Fig. 3). In addition a typical intermediate region has a reflectance spread of about 30% around its average value (McCord et al., 2012 Fig. 4), hence a reflectance value at least 15% lower than the local average is outside the reflectance range corresponding to an intermediate region, i.e., it is a dark unit. When the reflectance deviation from the local average is two times this threshold (i.e., 30%), we label the corresponding region as VDM.

The catalogue of DM units, with the relative geological context and spectral properties is listed in Table 1.

4.2. DM general properties

In addition to a broad equatorial low-albedo area located between 75°E and 150°W , observed and analyzed in detail by McCord et al. (2012) and Jaumann et al. (2014), 123

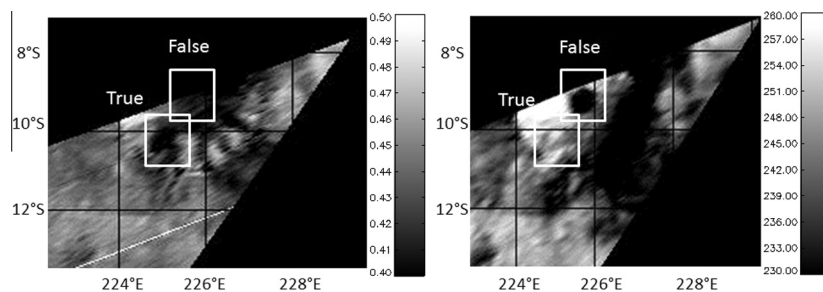


Fig. 1. False and genuine DM detection. VIR infrared ($1.2 \mu\text{m}$; left) and temperature frame (right) relative to the region at $8\text{--}12^\circ\text{S}$ and $224\text{--}228^\circ\text{E}$. The right squared region in both the frames is a false DM detection, a possible dark unit which is darker but cooler than the surroundings. The left squared region is a real DM detection. Here the darker areas are also hotter than the surroundings.

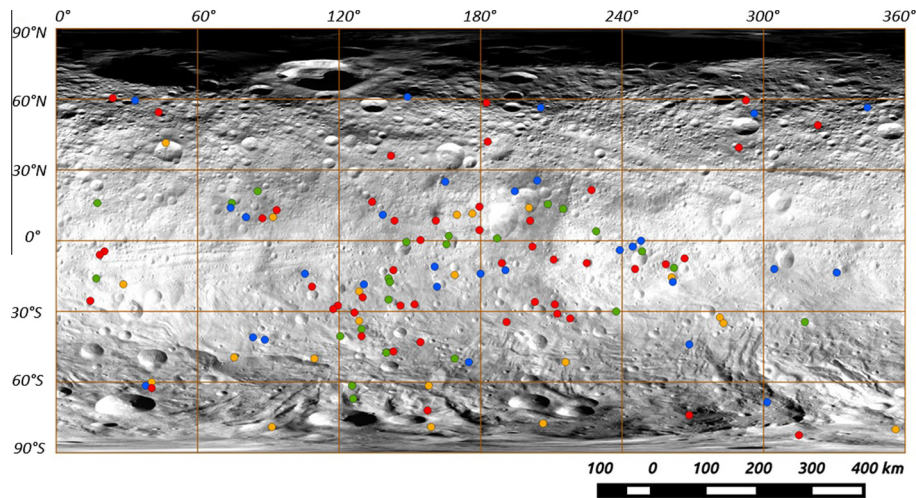


Fig. 2. Distribution on Vesta of dark material units. Each dot super-imposed on the Vesta FC map is a DM. Colours are associated to different geological features: blue = areal features, yellow = linear features, green = craters; red = ejecta. (For interpretation of the references to colour in this figure legend, the reader is referred to the web version of this article.)

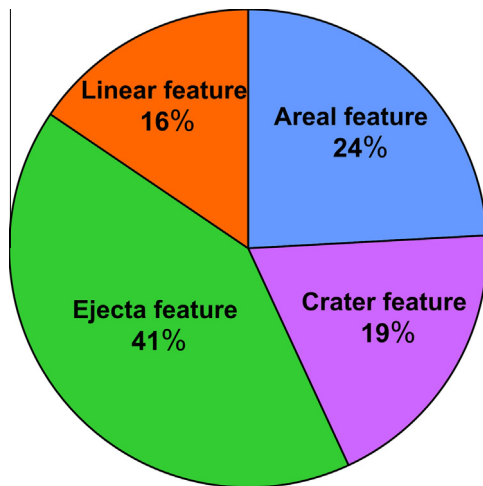


Fig. 3. Pie diagram. Illustrating the statistical distribution of the different DM families on Vesta.

well-defined DM units with different degrees of darkness were found, i.e. photometrically-corrected reflectance (calculated at $1.2\ \mu\text{m}$) spanning from 0.16 to 0.26. Their spatial distribution (Fig. 2) is quite uneven, with some Vestan regions hosting both DM and BM (e.g. Li et al., submitted for publication).

A large number of DM units (i.e. about 20) is located in the region limited by the Helena (41°S , 122°E), Serena (20°S , 120°E), Octavia (3°S , 147°E), Sextilia (39°S , 146°E) and Fonteia (53°S , 141°E) craters. Dark material found here is mainly of subsurface origin, as inferred by the fact that most DM units are dark outcrops from craters (Jaumann et al., 2014), even if ejecta and areal features are also observed. Also most of the bright units present in this area are associated with crater wall/scarp materials. In addition, this region is one of the most OH-enriched of the whole Vesta surface, since it is part of the Water Rich Terrain 1 observed by De Sanctis et al. (2012b).

Other DM units are grouped around well-known Vesta features located at equatorial latitudes, such as Aricia Tholus ($5\text{--}15^\circ\text{N}$ latitudes, $155\text{--}165^\circ$ longitudes), as well as the Marcia and Calpurnia craters ($185\text{--}205^\circ$ longitudes). These features are characterized

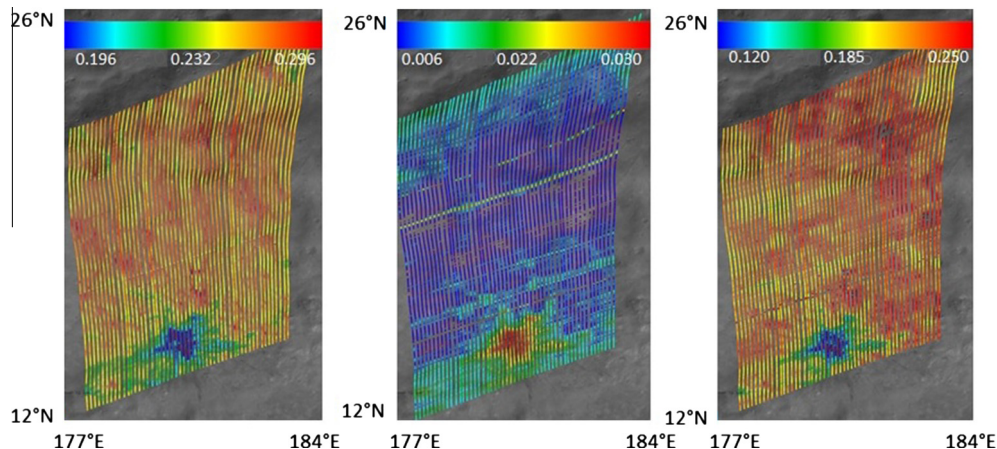


Fig. 4. VD3 deposit. Reflectance (left), OH-band depth (center) and Band II depth (right) maps overlapped to the Framing Camera mosaic (Jaumann et al., 2012). All the maps are projected on the Vesta Digital Terrain Model.

Table 1

List of dark material units found on the Vesta surface, with related geographic, geometric and spectral information. “Lab” indicates the label given to each unit and is given by D (for dark deposits) or VD (for very dark deposits) with a cardinal number increasing from high to low latitudes. “LatMin”, “LatMax”, “LngMin” and “LngMax” identifies the coordinates which include the unit. “Type” is the geomorphologic family (E for ejecta, AF for areal features, CR–CF–CW for crater rims, floors and walls, respectively – combination of them are possible – LF for linear features). “Cam” indicates if the feature is present also in the FC dark units catalogue; “Cov” is the coverage (% of detections ratioed on total number of observations). “AlbIR”, “AlbVIS”, “BCI”, “BCII”, “BDI”, “BDII”, “BAR”, “BHWII”, “OHband” are the values averaged on the dark area of 30° albedo at 1.2 μm, 30° albedo at 0.75 μm, Band I Center, Band II Center, Band I Depth, Band II Depth, BAR, Band II Half-width half maximum, band depth at 2.8 μm; “SD” gives the respective standard deviations. Finally, “Comp” is the unit composition (H for howarditic, E for eucritic, D for diogenitic – combinations of them are possible).

Lab	LatMin	LatMax	LngMin	LngMax	Type	Cam	Cov	AlbIR	SD	AlbVIS	SD	BCI	SD	BCII	SD	BDI	SD	BDII	SD	BAR	SD	BHWII	SD	OHband	SD	Comp
D1	60	61	23.5	25.5	E	n	100	0.21	0.01	0.146	0.01	0.94	0	1.98	0	0.39	0.03	0.16	0.01	1.7	0.2	0.23	0.05	0.019	0	E
D2	60.5	61.5	148.5	149.5	AF	n	100	0.19	0.01	0.125	0.02	0.94	0.02	2	0.02	0.29	0.05	0.07	0.02	1.6	0.4	0.23	0.06	0.024	0.01	E
D3	59	60	32	35	AF	n	100	0.2	0.01	0.131	0.01	0.94	0	1.99	0.02	0.31	0.03	0.09	0.02	1.6	0.3	0.25	0.04	0.02	0	E
D4	59	60	290	295	E	n	100	0.21	0.01	0.133	0.01	0.94	0	1.97	0	0.39	0.03	0.15	0.01	1.9	0.2	0.26	0.01	0.017	0	E
D5	58	59	181	184	E	n	50	0.21	0.01	0.13	0.01	0.94	0	1.99	0.01	0.37	0.03	0.12	0.01	1.9	0.2	0.26	0.01	0.018	0	E
D6	56.5	57.5	204	207	AF	n	14	0.21	0.02	0.134	0.02	0.94	0.01	1.99	0.01	0.42	0.03	0.17	0.01	1.8	0.3	0.25	0.02	0.016	0	E
VD1	56	57	343	345	AF	n	33	0.15	0.03	0.108	0.04	0.94	0.01	1.98	0.01	0.45	0.12	0.17	0.03	1.7	0.4	0.13	0.11	0.014	0	E
D7	54	55	42	45	E	n	40	0.2	0.01	0.136	0.01	0.94	0	1.99	0	0.31	0.02	0.1	0.01	1.4	0.1	0.19	0.03	0.031	0	E
D8	53	55	292	300	AF	n	25	0.22	0.01	0.144	0.01	0.94	0	1.99	0	0.39	0.02	0.15	0.01	1.6	0.1	0.23	0.02	0.016	0	E
D9	48.5	49.5	322	324	E	n	50	0.21	0.01	0.151	0.01	0.94	0	1.98	0.01	0.37	0.02	0.17	0.01	1.8	0.2	0.22	0.03	0.015	0	E
D10	41	42	46	47	CR	n	33	0.22	0.01	0.156	0.01	0.94	0	1.99	0.01	0.3	0.01	0.11	0.01	1.5	0.1	0.17	0.05	0.032	0	E
D11	41	43	182	183.5	E	n	100	0.23	0	0.164	0.01	0.94	0	1.99	0	0.37	0.01	0.16	0.01	1.6	0.1	0.22	0.02	0.018	0	E
D12	39	40	298	299	E	n	33	0.22	0	0.164	0.01	0.93	0	1.97	0	0.38	0.01	0.18	0.01	1.9	0.1	0.23	0.03	0.017	0	E
D13	35	37	140	144	E	y	29	0.22	0	0.151	0.01	0.93	0	1.98	0	0.33	0.01	0.14	0.01	1.8	0.1	0.21	0.02	0.023	0	E
VD2	24	27	201	207	AF	n	50	0.19	0.01	0.129	0.01	0.93	0	1.99	0	0.35	0.02	0.15	0	1.8	0.2	0.19	0.03	0.023	0	E
D14	24	25.5	164	166	AF	n	100	0.2	0.01	0.14	0.01	0.94	0	2	0.01	0.35	0.01	0.15	0.01	1.6	0.1	0.2	0.03	0.021	0	E
D15	20	23	226	228	E	n	20	0.2	0	0.145	0.01	0.94	0	1.99	0.01	0.34	0.02	0.15	0.01	1.6	0.2	0.19	0.02	0.021	0	E
D16	20	22	194	195	E	y	50	0.2	0	0.115	0	0.93	0	1.99	0	0.28	0.01	0.13	0.01	2.1	0.1	0.18	0.03	0.026	0	E
D17	20	22	85	86	CS	n	43	0.2	0	0.14	0	0.94	0	1.98	0	0.37	0.01	0.16	0	1.7	0.1	0.23	0.02	0.022	0	E
D18	15	17	74	75	CR	n	40	0.2	0	0.143	0	0.94	0	1.98	0	0.37	0.01	0.15	0.01	1.5	0.1	0.2	0.03	0.024	0	E
D19	15.5	16.5	17	18	CF	n	20	0.21	0.01	0.134	0.01	0.94	0.01	1.97	0.01	0.46	0.05	0.19	0.01	2.1	0.3	0.28	0.01	n/a	n/a	E
D20	15	18	131	137	E	y	10	0.2	0.01	0.137	0.01	0.93	0	2	0.03	0.36	0.03	0.18	0.01	2	0.2	0.2	0.04	0.021	0	E
VD3	14	15	179	180	E	y	60	0.2	0	0.142	0	0.93	0	1.99	0	0.3	0	0.14	0.01	1.7	0.1	0.19	0.02	0.031	0	E
D21	13	15	200	201	WM	n	30	0.2	0	0.138	0	0.93	0	1.99	0	0.37	0.01	0.16	0.01	1.6	0.1	0.19	0.03	0.023	0	E
D22	13	15	73	75.5	AF	n	33	0.21	0.01	0.138	0.01	0.93	0	1.97	0.01	0.41	0.01	0.18	0.01	1.6	0.1	0.26	0.01	0.017	0	E
D23	13	14	214	215.5	CR	n	50	0.19	0	0.135	0	0.94	0	1.99	0	0.33	0.01	0.14	0	1.5	0.1	0.18	0.02	0.027	0	E
VD4	13	18	206	213	CS	n	67	0.2	0	0.138	0	0.94	0	1.99	0	0.36	0	0.15	0	1.6	0	0.18	<	0.024	0	E
D24	12.5	13.5	93	94	E	n	50	0.19	0	0.127	0.01	0.93	0	1.98	0	0.36	0.01	0.16	0	1.6	0.1	0.22	0.02	0.026	0	E
D25	11	12	175	178	LF	y	9	0.22	0	0.16	0.01	0.94	0	2	0.03	0.38	0.01	0.18	0.01	1.6	0.1	0.21	0.03	0.022	0	E
D26	10	12	168	172	LF	y	21	0.2	0	0.147	0	0.94	0	1.99	0	0.35	0.01	0.15	0.01	1.5	0.1	0.18	0.02	0.025	0	E
D27	10	12	137	140	AF	y	71	0.19	0	0.13	0	0.94	0	1.99	0	0.34	0.01	0.15	0	1.6	0.1	0.18	0.02	0.029	0	E
D28	9	11	79	82	AF	n	10	0.21	0.01	0.125	0.01	0.93	0	1.98	0.01	0.4	0.01	0.17	0	1.7	0.1	0.25	0.02	0.016	0	H/E
D29	9	11.5	91	93	LF	y	50	0.19	0	0.133	0	0.93	0	1.98	0	0.37	0.01	0.16	0	1.6	0.1	0.23	0.01	0.024	0	H/E
D30	9	10	87	88	E	n	57	0.19	0.01	0.129	0.01	0.93	0	1.98	0	0.39	0.01	0.17	0	1.6	0.1	0.23	0.01	0.022	0	H/E
VD5	8	11	158.5	163	E	y	75	0.19	0	0.136	0	0.93	0	1.99	0	0.29	0.01	0.13	0.01	1.6	0.1	0.17	0.02	0.033	0	E
D31	7	10	142	145	E	y	24	0.18	0	0.122	0.01	0.94	0	1.99	0	0.36	0.01	0.15	0.01	1.6	0.1	0.16	0.01	0.025	0	E
D32	6	11	197	205	E	n	60	0.19	0	0.129	0	0.93	0	1.99	0	0.36	0	0.15	0	1.6	0	0.18	0.01	0.021	0	E
D33	4	5	179	180	E	y	50	0.21	0	0.151	0	0.93	0	1.99	0	0.36	0	0.18	0	1.6	0.1	0.2	0.02	0.021	0	E
D34	3.5	4.5	228.5	229.5	CR	y	14	0.22	0	0.16	0.01	0.93	0	1.98	0.01	0.36	0.01	0.16	0	1.5	0.1	0.19	0.02	0.022	0	E
VD6	0	4	165	168	CR	y	50	0.19	0.01	0.132	0.01	0.93	0	1.99	0	0.36	0.01	0.15	0.01	1.4	0	0.18	0.02	0.027	0	E
D35	0	2	186	188	CR	n	25	0.22	0.01	0.159	0.01	0.93	0	1.99	0.01	0.35	0.02	0.17	0.02	1.9	0.1	0.21	0.03	0.019	0	E
D36	−1	0	148	149	CR	y	28	0.17	0.01	0.116	0.01	0.93	0	1.99	0	0.36	0.01	0.16	0.01	1.7	0.1	0.2	0.02	0.025	0	E
D37	−1	1	247	249	AF	n	12	0.24	0	0.174	0.01	0.93	0	1.98	0.01	0.39	0.01	0.2	0.01	1.9	0.1	0.25	0.02	0.015	0	E
D38	−2	−1	165	166	CR	y	33	0.18	0.01	0.133	0.01	0.94	0	1.99	0	0.36	0.01	0.14	0.01	1.3	0.1	0.16	0.02	0.026	0	E
D39	−3	−2	244	245	AF	n	20	0.2	0.01	0.137	0.01	0.93	0	1.99	0	0.36	0.01	0.16	0.01	1.9	0.1	0.17	0.01	0.019	0	E
D40	−4	−1	201	203	E	y	67	0.2	0	0.14	0	0.93	0	1.99	0	0.35	0.01	0.15	0	1.6	0.1	0.18	0.01	0.021	0	E
D41	−5	−3.5	237.5	241	AF	n	40	0.23	0	0.167	0	0.94	0	1.98	0	0.39	0.01	0.18	0	1.7	0.1	0.23	0.02	0.017	0	E
D42	−5.5	−3.5	20	21	E	y	16	0.22	0.02	0.162	0.02	0.94	0	1.98	0.01	0.37	0.02	0.17	0.02	1.7	0.2	0.24				

Table 1 (continued)

Lab	LatMin	LatMax	LngMin	LngMax	Type	Cam	Cov	AlbIR	SD	AlbVIS	SD	BCI	SD	BCII	SD	BDI	SD	BDII	SD	BAR	SD	BHWII	SD	OHband	SD	Comp
D59	-18	-17	140.5	142	CR	y	33	0.19	0	0.134	0	0.93	0	1.99	0	0.37	0	0.17	0.01	1.6	0	0.2	0.03	0.024	0	E
D60	-18	-17	216	217	AF	n	16	0.23	0	0.171	0.01	0.93	0	1.98	0	0.37	0.01	0.19	0.01	1.9	0.1	0.22	0.02	0.02	0	E
D61	-19	-18	28	29	LF	y	33	0.24	0	0.176	0	0.93	0	1.97	0	0.41	0	0.21	0	1.8	0	0.25	0.01	0.016	0	H/E
D62	-20	-17	129	132	AF	y	70	0.19	0.01	0.14	0	0.93	0	1.98	0	0.34	0.01	0.17	0.01	1.6	0.1	0.21	0.02	0.026	0	E
D63	-20	-19	108	109	E	y	14	0.19	0.01	0.136	0.01	0.94	0	1.98	0	0.38	0.01	0.16	0.01	1.5	0.1	0.25	0.02	0.026	0	H/E
D64	-20	-19	161	162	AF	y	50	0.19	0	0.135	0.01	0.93	0	1.99	0	0.34	0.01	0.14	0.01	1.5	0.1	0.15	0.01	0.023	0	E
D65	-22	-21	128	129	LF	y	43	0.2	0	0.132	0	0.93	0	1.98	0	0.36	0.01	0.18	0	1.8	0.1	0.25	0.01	0.022	0	E
D66	-25.5	-23	128.5	131	E	y	56	0.18	0	0.131	0.01	0.93	0	1.99	0	0.36	0.01	0.16	0	1.7	0.1	0.21	0.02	0.022	0	E
D67	-26	-24	140	142	CR	y	50	0.18	0.01	0.134	0.01	0.93	0	1.99	0	0.36	0.01	0.16	0.01	1.6	0.1	0.2	0.02	0.03	0	E
D68	-26	-25	14	15	E	y	40	0.23	0.01	0.157	0.01	0.94	0	1.97	0.01	0.39	0.02	0.2	0.01	1.7	0	0.26	0	0.018	0	E
D69	-27.5	-26.5	151.5	152.5	E	y	33	0.19	0.01	0.139	0.01	0.93	0	1.98	0	0.35	0.01	0.17	0.01	1.6	0.1	0.22	0.02	0.026	0	E
D70	-28	-26	211	212	E	y	16	0.23	0	0.168	0	0.94	0	1.98	0	0.4	0.01	0.19	0.01	1.6	0.1	0.25	0.02	0.013	0	E
VD11	-28	-27	119	120	E	y	43	0.19	0.01	0.131	0.01	0.93	0	1.97	0	0.36	0.01	0.16	0.01	1.7	0.1	0.23	0.01	0.025	0	H/E
D71	-29	-26	144	148	E	y	36	0.2	0	0.142	0	0.94	0	1.99	0	0.37	0.01	0.17	0	1.5	0	0.21	0.01	0.025	0	E
D72	-30	-22	196	210	E	n	43	0.22	0	0.161	0	0.93	0	1.98	0	0.4	0	0.18	0	1.6	0	0.24	0.01	0.012	0	E
D73	-30	-29	154	155	E	y	32	0.2	0	0.146	0	0.93	0	1.98	0	0.38	0	0.17	0	1.8	0	0.24	0.01	0.019	0	E
D74	-30	-28.5	117	118	E	y	38	0.2	0	0.145	0.01	0.93	0	1.97	0	0.38	0.01	0.19	0.01	1.7	0.1	0.25	0.01	0.026	0	H/E
D75	-30.5	-29.5	237	238	F	n	20	0.24	0	0.18	0	0.94	0	1.98	0	0.35	0	0.17	0	1.8	0	0.22	0	0.02	0	E
D76	-31	-30	126	127	E	y	40	0.18	0.01	0.155	0.02	0.93	0	1.98	0.01	0.34	0.01	0.19	0.01	1.7	0.1	0.26	0.01	0.029	0	H/E
D77	-31.5	-30.5	212	213	E	n	20	0.23	0	0.177	0.01	0.93	0	1.98	0	0.38	0.01	0.19	0	1.6	0.1	0.24	0.02	0.009	0	H/E
D78	-33.5	-32	281	282.5	LF	y	75	0.22	0.01	0.169	0.01	0.93	0	2	0.01	0.38	0.01	0.18	0.01	1.4	0.1	0.19	0.01	0.009	0	E
D79	-33.5	-32.5	217.5	218.5	E	n	12	0.23	0	0.177	0	0.94	0	1.98	0.01	0.37	0.01	0.19	0.01	1.8	0.1	0.23	0.03	0.014	0	E
D80	-34.5	-33.5	128	129	LF	n	14	0.24	0.01	0.17	0.01	0.93	0	1.99	0	0.39	0.01	0.17	0.01	1.7	0.1	0.27	0.01	0.017	0	E
D81	-35	-34	317	318	CW	n	14	0.23	0.01	0.188	0.01	0.93	0	1.98	0	0.35	0.01	0.16	0.01	1.4	0.2	0.24	0.03	0.012	0	H/E
D82	-36	-33	188	194	E	n	20	0.23	0	0.174	0	0.93	0	1.98	0	0.4	0	0.19	0.01	1.7	0.1	0.24	0.02	0.014	0	E
D83	-37	-33	281	285	LF	y	27	0.22	0.01	0.169	0.01	0.93	0	2	0.01	0.37	0.01	0.17	0.01	1.4	0.1	0.19	0.01	0.009	0	E
D84	-38	-37	129	130	CR	y	14	0.2	0	0.135	0	0.94	0	1.99	0.01	0.34	0.01	0.12	0.01	1.5	0.1	0.22	0.03	0.025	0	E
D85	-41	-38	126	131	E	y	62	0.2	0	0.142	0	0.93	0	1.97	0	0.4	0.01	0.19	0	1.7	0	0.25	0.01	0.025	0	H/E
D86	-41	-40	120	121	CR	y	20	0.2	0	0.14	0.01	0.93	0	1.97	0.01	0.39	0.01	0.19	0.01	1.8	0.1	0.26	0.01	0.023	0	H/E
D87	-42	-40	82	85	AF	n	12	0.27	0.01	0.189	0.03	0.93	0.01	1.97	0	0.46	0.09	0.23	0.01	1.8	0.2	0.26	0.01	0.013	0	H/E
VD12	-43	-41	87	90	AF	n	25	0.21	0	0.178	0	0.93	0	1.98	0	0.42	0.01	0.2	0.01	1.8	0.1	0.27	0	0.012	0	H/E
D88	-43.5	-42	154	155	E	y	67	0.2	0.01	0.128	0.01	0.94	0	1.98	0	0.38	0.02	0.18	0.02	2	0.1	0.25	0.01	0.02	0	H/E
D89	-45	-43	267	270	AF	n	33	0.23	0	0.171	0	0.94	0	1.99	0	0.42	0	0.22	0	1.7	0	0.26	0.02	0.013	0	E
VD13	-48	-46	142	144	E	y	80	0.21	0.01	0.147	0.01	0.93	0	1.98	0	0.39	0.01	0.18	0.01	1.6	0.1	0.26	0.01	0.025	0	E
VD14	-49	-46	138	142.5	CR	y	88	0.21	0.01	0.145	0.01	0.93	0	1.98	0	0.4	0.01	0.19	0.01	1.6	0.1	0.25	0.01	0.021	0	E
D90	-50	-49	75	76	LF	n	40	0.24	0.01	0.191	0.01	0.93	0	1.95	0	0.48	0.01	0.32	0	2.3	0.1	0.3	0.01	n/a	n/a	H
VD15	-50.5	-49.5	169.5	170.5	CR	y	40	0.21	0	0.156	0.01	0.93	0	1.97	0	0.39	0.01	0.19	0	1.7	0.1	0.26	0.01	0.023	0	H/E
D91	-51	-49	109	110.5	LF	n	14	0.2	0.01	0.142	0.04	0.94	0.01	1.98	0.01	0.45	0.07	0.23	0	1.8	0.1	0.26	0.02	0.012	0	E
D92	-52	-51	215.5	216.5	LF	n	14	0.24	0.01	0.187	0.02	0.93	0	1.98	0	0.42	0.03	0.23	0	1.8	0.2	0.27	0.01	0.01	0	E
D93	-52	-51	174.5	175.5	AF	n	16	0.21	0.01	0.153	0.01	0.93	0	1.99	0.01	0.38	0.01	0.2	0.02	2	0.3	0.27	0.01	0.019	0.01	E
VD16	-61	-59	39.5	41.5	LF	n	33	0.25	0.01	0.171	0.01	0.93	0	1.98	0.01	0.39	0.01	0.25	0	2	0.1	0.28	0.01	0.01	0.01	H/E
D94	-62	-61	200	204	LF	y	50	0.23	0.01	0.123	0	0.93	0	1.96	0	0.45	0.01	0.31	0.01	1.8	0.1	0.3	0.01	0.011	0	H/E
D95	-62	-61	37	38.5	AF	n	33	0.24	0.01	0.176	0.01	0.93	0	1.97	0.01	0.43	0.02	0.25	0	1.9	0.1	0.27	0.01	0.012	0	E
D96	-62	-61	125	126	CR	n	33	0.22	0	0.218	0	0.93	0	1.96	0	0.44	0	0.27	0	1.4	0	0.29	0	0.014	0	H/E
D97	-63	-62	40	41	E	n	25	0.2	0.04	0.163	0.05	0.98	0.08	1.97	0.01	0.48	0.07	0.27	0.02	1.9	0.4	0.24	0.08	n/a	n/a	H/E
VD17	-69	-65	124	128	F	n	80	0.22	0.01	0.168	0.01	0.93	0	1.98	0.01	0.36	0.02	0.16	0.01	1.3	0.1	0.24	0.02	0.009	0	H/E
D98	-70	-67	300	303	AF	n	20	0.09	0.02	0.088	0.09	1.02	0.08	1.98	0.02	0.71	0.17	0.3	0.02	1.8	0.5	0.21	0.11	0.012	0	H/E
D99	-73	-71.5	157	158	E	n	33	0.22	0	0.186	0	0.92	0	1.97	0	0.46	0	0.28	0	1.8	0	0.3	0	0.012	0	H/E
D100	-74.5	-73.5	268	269	E	n	33	0.22	0.01	0.168	0.01	0.93	0	1.97	0.01	0.45	0.02	0.24	0.01	1.7	0.1	0.26	0.01	0.012	0	H/E
D101	-78	-77	206	207	LF	n	50	0.24	0	0.177	0.01	0.93	0	1.98	0	0.45	0.01	0.25	0.01	1.7	0.1	0.27	0.01	0.006	0	H/E
D102	-79.5	-78	158	160	LF	n	14	0.26	0.01	0.184	0.01	0.94	0	1.97	0	0.44	0.01	0.22	0.01	1.7	0.1	0.28	0.01	0.009	0	E
D103	-80	-78	88	95	LF	n	11	0.24	0.01	0.175	0.02	0.93	0	1.94	0.01	0.53	0.02	0.34	0	2.2	0.2	0.3	0	n/a	n/a	H
VD19	-80.5	-79.5	355.5	357	LF	n	33	0.24	0.02	0.174	0.03	0.93	0	1.97	0.01	0.47	0.05	0.26	0.01	1.8	0.2	0.28	0.01	0.007	0	H/E
D104	-83	-82	314	316	E	n	12	0.21	0.02	0.166	0.03	0.98	0.08	1.99	0.02	0.37	0.05	0.22	0.02	1.9	0.4	0.23	0.08	0.016	0.01	E

by a mixture of bright and dark materials (Li et al., 2013). The Aricia dark unit was generated by an impact event which excavated dark material; Marcia is a large impact feature that is dominated by material that experienced mass wasting from a dark layer inside the crater and accumulated on a plateau above the crater floor, whereas the dark material in Calpurnia crater is a dark avalanche (Jaumann et al., 2014). The characteristics of DM in the region between Cornelia and Numisia craters (latitudes 14°S–6°N and longitudes 219–254°), whose detailed albedo map as inferred by VIR data can be found in Longobardo et al. (2014), suggest that dark material was mixed in the regolith by preexisting impacts (Jaumann et al., 2014) and then excavated by these two major craters. A more detailed analysis of the Numisia ejecta is given below.

Other small groups of DM are observed at low longitudes (10–45°), around the Rubria and Occia craters (30°S–0° latitudes) and around Tarpeia (60°S), and between Geganina and Eutropia

(longitudes 60–100° and latitudes 5–25°N). Otherwise, sparse (i.e., not grouped) DM is located at higher and lower latitudes.

depressions or dome margins, lineaments, scarp bases or crests, and troughs (Jaumann et al., 2012). Finally, areal features include mantling material, patterned ground, secondary crater chains and hummocky terrains (Jaumann et al., 2012). Statistically, the taxonomy of the dark material units is well represented as shown in Fig. 3 and is dominated by the ejecta (about 40% of the total units) whereas the other three families, linear feature, crater-associated feature and areal feature, are nearly equally represented in the DM.

4.3. Spectral parameters mapping of the different DM families

VD3 unit (Fig. 4) is an example of the first DM family and it is a dark ejecta, generated by a small unnamed impact crater in the

Aricia Tholus region (Jaumann et al., 2014). It extends across latitudes 14–15°N and longitudes 179–180° and has been detected in six observations. The unit has an eucritic composition, as revealed by the band centers analysis (see Table 1 and discussion in Section 5.1), and it is extremely rich in OH: the distribution maps of OH and albedo (or band depth II), appear to be anti-correlated, a common behavior for every DM deposit (see Figs. 4–6).

VD7 (ranging from 3°S to 6°S latitudes and 247° to 250° longitudes) is a sample of the crater associated DM units and corresponds to the Numisia (eucritic) crater rim (Fig. 5). The very dark material present here originated from the dark subsurface layer which is exposed in the northern crater wall (Jaumann et al., 2014). This DM is one of the most observed by VIR (eight

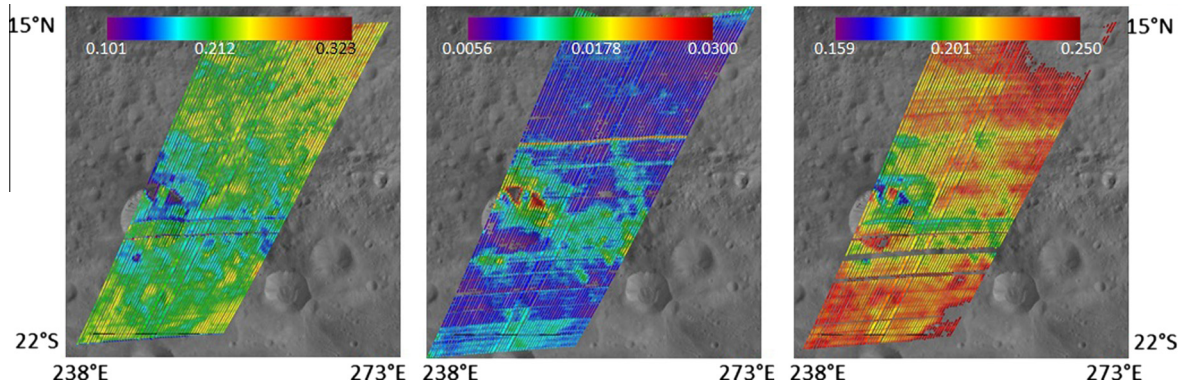


Fig. 5. VD7 deposit. Reflectance (left), OH-band depth (center) and Band II depth (right) maps overlapped to the Framing Camera mosaic (Jaumann et al., 2012). All the maps are projected on the Vesta Digital Terrain Model.

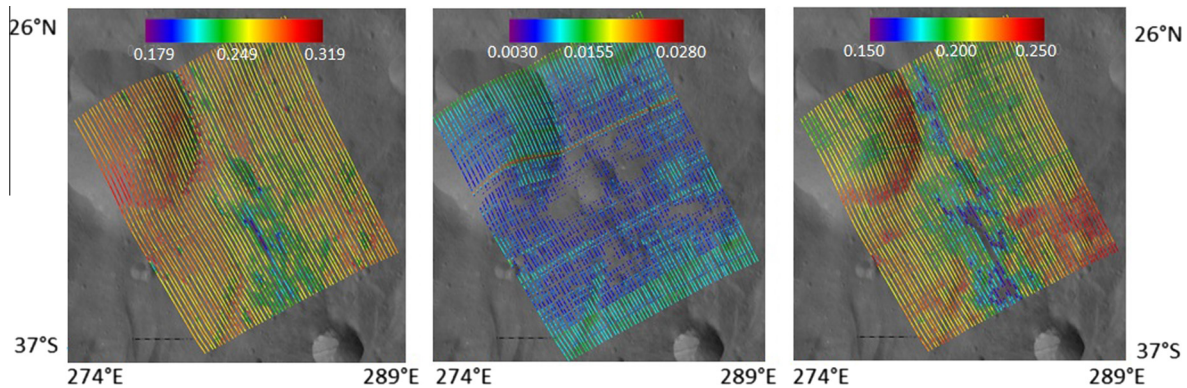


Fig. 6. D54 deposit. Reflectance (left), OH-band depth (center) and Band II depth (right) maps overlapped to the Framing Camera mosaic (Jaumann et al., 2012). All the maps are projected on the Vesta Digital Terrain Model.

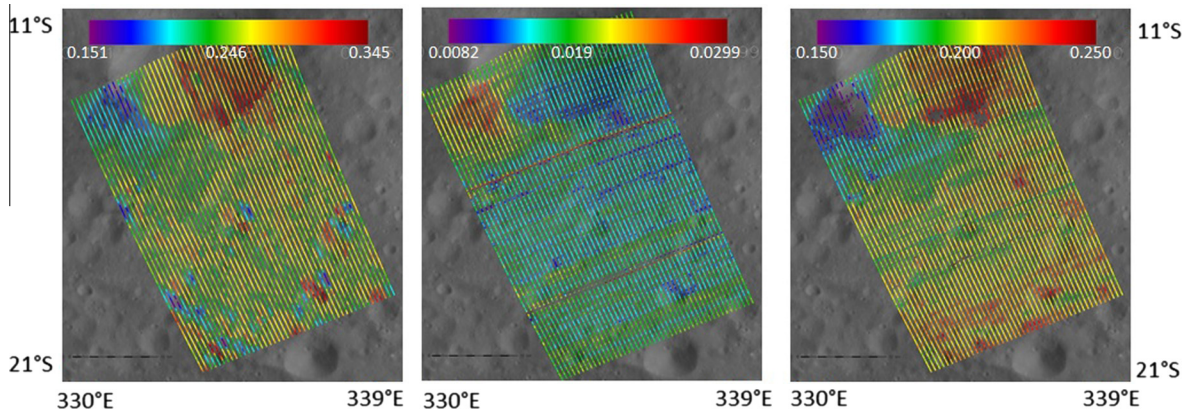


Fig. 7. D83 deposit. Reflectance (left), OH-band depth (center) and Band II depth (right) maps overlapped to the Framing Camera mosaic (Jaumann et al., 2012). All the maps are projected on the Vesta Digital Terrain Model.

hyperspectral images). Again the distribution maps show a very clear spatial anti-correlation between OH-band depth and albedo (or BDII).

Fig. 6 shows an example of an areal DM feature, the D54 unit, which extends from 12.5°S to 15°S latitudes and 330° to 332° longitudes. Also in this case the composition is eucrite-rich.

The linear feature D83 (Fig. 7), located at 33–37° latitudes and 281–285° longitudes, is eucritic, too. Interestingly and differently from the previous cases, in this unit there is not a local OH enrichment, as shown by the map distribution of the OH absorption band.

5. DM units: Composition and origin of the darkening

In order to understand the composition and the origin of the DM units a step by step process will be applied, beginning with the spectral comparison among the different DM families. A second step will be the study of the composition (eucritic–howarditic–diogenitic), followed by the analysis of grain size influence and finally by the interpretation of the causes at the origin of the darkening. Spectral parameters calculated on the VIR spectra and on HED or Vesta-relevant laboratory spectra will support this analysis.

Laboratory spectra of HEDs, mixtures of metal–pyroxene, eucrite–carbonaceous chondrite, were collected from the RELAB database or provided by the HOSERLab at the University of Winnipeg's (see Table 2 for details).

Firstly, we compare a typical spectrum of Vesta with dark and bright material unit spectra. Excluding the obvious difference in the overall albedo, all the spectra show the same absorption bands. We did not find any DM spectra that exhibit any additional major spectral feature other than the 0.9 and 1.9 μm ones, even though a weak 2.8 μm feature is frequently observed. This strong indication suggests a DM composition similar to the average Vestan material, i.e. pyroxene-rich material such as an HED.

In general, all the analyzed DM show a 40–50% decrease in both the band I and Band II depths, with respect to the BM (Fig. 8). The most variable parameter is the BAR, ranging from 1.4 to 2.2; however all these observed values are fully compatible with the BAR retrieved for a very large set of HEDs (e.g. Moskovitz et al., 2010).

The different DM geological families show similar spectral properties, with an average eucritic composition (see subsection 5.1), band depths between 0.4–0.5 (Band I) and 0.15–0.20 (Band II), Band II HWHM between 0.17 and 0.30, and OH band depth between 0.01 and 0.03. The dark units associated with linear features are slightly brighter than the other DM units (Fig. 9), and this is reflected also in the deeper band depths (with BI and BII depth usually larger than 0.38 and 0.18 respectively), in the larger band II HWHM (between 0.25 and 0.30) and in the lowest OH presence (band depth around 0.01). In addition, they are on average the most howardite-rich samples among the DM units, (see the next subsection). The slight difference between linear features and other DMs can be explained by the fact that the former are mainly located at low latitudes, where reflectance is on average larger and therefore areas detected as dark material units could have a larger absolute reflectance, as is observed. This means that DM linear features can be considered a mixture of less dark and brighter background material that produces slightly brighter and OH-poor DM units.

5.1. Composition

An attempt to explore more precisely the compositional variability of DM within the HED family can be done by plotting the Band I Center versus Band II Center, which is generally used as a compositional plot because it shows a clear trend from diogenites

to eucrites (e.g. Gaffey, 1976; De Sanctis et al., 2013; McSween et al., 2011).

In Fig. 10 we plotted the BCI versus BCII for all the DM listed in the catalogue in comparison with bright unit samples listed in Zambon et al. (this issue) and HEDs from Table 2. Following the definition of De Sanctis et al. (2013), the majority of the Vesta surface is howarditic/eucritic to eucritic. The DM units and the BM units overlay in the same scatterplot region, similarly to typical Vesta, even if the dark materials are on average more eucritic. As a matter of fact, the percentage of eucritic DM units is 72% whereas it is 55% for BM units (Zambon et al., this issue). In addition, in contrast to what is observed for BM, no dark diogenitic units have been observed.

5.2. Grain size effect

An increase in grain size produces a decrease in reflectance and an increase in band depth (Cloutis et al., 2013). The BDI versus BDII plot of DM units (Fig. 8) is very interesting and shows shallower band depths for DM units with respect to BM units, indicating smaller grain size for DM units, as suggested by the behavior of the HED on the same plot. Nevertheless, the low reflectances of DM units would indicate relatively large grain size, as opposed to what is suggested from the analysis of the band depths. The addition of an increasing abundance of carbonaceous chondrite or metal in a pyroxene-rich material has the same effect of reducing both the reflectance (as expected) and the band depths. Combining the reflectance and the BD in a scatterplot allows us to disentangle the changing grain size from the darkening agent effects. The behavior of the reflectance versus BDI or BDII are practically identical, therefore we select BDII versus reflectance scatterplot (Fig. 11a and b); to analyze in detail the different behaviors. In order to have a close comparison with the typical Vestan material we selected here only eucrite and howardite samples, omitting diogenite samples, as the diogenitic material is more sporadic on Vesta (De Sanctis et al., 2012a, 2013) and absent on Vesta DM units. Five eucrites and one howardite are available in four size intervals (0–25, 25–45, 45–75, 75–125 μm), two eucrites in the intervals (0–25, 25–45 μm), and two eucrites and three howardites in the smallest size interval only. For each meteorite sample, there is a common behavior in the scatterplot as the grain size decreases, i.e., the reflectance increases and the BDII decreases, as indicated by the arrow (from the upper left to the bottom right).

The 0–25 μm and the 25–45 μm grain size clusters (light blue and pink ellipses, respectively) show a very interesting behavior. There are eight eucrite/howardite samples that have points in both the dimensional intervals and for each sample the distance between these points in the BDII–reflectance plane is very similar. For each dimensional interval, six out of eight of these HED samples behave in a quasi-linear way with the exception of the howardite EET83376 (black filled diamonds) and the eucrite ALHA76005 (blue filled squares). The 0–25 and 25–45 points for these two samples seem to have a smaller band depth and lower reflectance than the other samples, being located away from the others and from their linear behavior towards the direction of smaller grain size (see the dimensional arrow). We believe that the most reasonable explanation for this peculiarity stands in the production of the fine-grained samples from the bulk meteorite; in fact it is possible that the apparent decreasing of grain size for EET83376 and ALHA76005 could be due to the increasing in the grinding time of the bulk specimens. While a dedicated experiment could better address this aspect, our intent here is to try to define a dimensional domain in the BDII–reflectance plane identifying dimensional size boundary. For this purpose we discarded the points of these two samples, defining with a good approximation the linear boundaries

Table 2

List of meteorite samples used in this work, with grain size and related spectral parameters: reflectance, band centers (BCI, BCII) and band depth (BDI, BDII).

Type	Name	Grain size (μm)	Reflectance (1.2 μm)	BCI	BCII	BDI	BDII	Reference
Diogenite	A-881526	0–25	0.631	0.920	1.875	0.651	0.414	RELAB
Diogenite	EETA79002	0–25	0.430	0.920	1.890	0.507	0.294	RELAB
Diogenite	EETA79002	25–45	0.288	0.920	1.885	0.652	0.442	RELAB
Diogenite	EETA79002	45–75	0.264	0.920	1.880	0.648	0.470	RELAB
Diogenite	EETA79002	75–125	0.224	0.915	1.885	0.624	0.472	RELAB
Diogenite	Johnstown	0–25	0.428	0.915	1.880	0.443	0.238	RELAB
Diogenite	Johnstown	25–45	0.374	0.915	1.885	0.634	0.440	RELAB
Diogenite	Tatahouine	0–25	0.656	0.920	1.890	0.638	0.405	RELAB
Diogenite	Y-74013	0–25	0.354	0.925	1.915	0.418	0.241	RELAB
Diogenite	Y-74013	25–45	0.317	0.920	1.900	0.611	0.415	RELAB
Diogenite	Y-75032	0–25	0.380	0.930	1.940	0.517	0.293	RELAB
Diogenite	Y-75032	25–45	0.229	0.925	1.940	0.671	0.455	RELAB
Eucrite	A-881819	0–25	0.535	0.930	1.950	0.481	0.273	RELAB
Eucrite	ALHA76005	0–25	0.561	0.935	1.970	0.385	0.224	RELAB
Eucrite	ALHA76005	25–45	0.416	0.940	1.965	0.496	0.351	RELAB
Eucrite	ALHA76005	75–125	0.270	0.945	1.945	0.535	0.440	RELAB
Eucrite	ALH-78132	0–25	0.491	0.935	1.955	0.426	0.256	RELAB
Eucrite	ALH-78132	25–45	0.323	0.935	1.945	0.589	0.411	RELAB
Eucrite	ALH-78132	45–75	0.252	0.935	1.935	0.626	0.478	RELAB
Eucrite	Juvinas	0–25	0.495	0.940	1.975	0.471	0.270	RELAB
Eucrite	Juvinas	25–45	0.359	0.945	1.950	0.600	0.417	RELAB
Eucrite	Juvinas	45–75	0.281	0.950	1.925	0.625	0.470	RELAB
Eucrite	Juvinas	75–125	0.217	0.955	1.905	0.615	0.483	RELAB
Eucrite	Macibini (with impact melt)	0–63	0.144	0.960	1.960	0.531	0.095	RELAB
Eucrite	Macibini	0–63	0.261	0.940	1.980	0.465	0.292	RELAB
Eucrite	Millbillillie	0–25	0.464	0.940	1.985	0.454	0.244	RELAB
Eucrite	Millbillillie	25–45	0.318	0.940	1.975	0.594	0.380	RELAB
Eucrite	Millbillillie	45–75	0.261	0.940	1.965	0.599	0.411	RELAB
Eucrite	Millbillillie	75–125	0.223	0.940	1.955	0.580	0.420	RELAB
Eucrite	Padvarnikai (with impact melt)	0–25	0.206	0.950	2.015	0.231	0.089	RELAB
Eucrite	Padvarnikai (with impact melt)	25–45	0.168	0.955	2.025	0.206	0.097	RELAB
Eucrite	Padvarnikai	0–25	0.417	0.940	1.985	0.469	0.256	RELAB
Eucrite	Padvarnikai	25–45	0.311	0.945	1.960	0.549	0.373	RELAB
Eucrite	Pasamonte	0–25	0.509	0.945	1.985	0.492	0.286	RELAB
Eucrite	Stannern	0–25	0.449	0.940	1.990	0.407	0.233	RELAB
Eucrite	Stannern	25–45	0.312	0.945	1.965	0.526	0.378	RELAB
Eucrite	Y-74450	0–25	0.386	0.935	1.975	0.379	0.187	RELAB
Eucrite	Y-74450	25–45	0.264	0.935	1.965	0.537	0.330	RELAB
Eucrite	Y-74450	45–75	0.216	0.935	1.960	0.574	0.391	RELAB
Howardite	EET83376	0–25	0.567	0.935	1.960	0.460	0.283	RELAB
Howardite	EET87503	0–25	0.431	0.930	1.945	0.378	0.192	RELAB
Howardite	EET87503	25–45	0.339	0.930	1.940	0.454	0.273	RELAB
Howardite	EET87503	45–75	0.241	0.930	1.930	0.498	0.354	RELAB
Howardite	EET87503	75–125	0.206	0.930	1.930	0.489	0.352	RELAB
Howardite	Petersburg	0–25	0.495	0.940	1.975	0.471	0.270	RELAB
Howardite	Y790727	0–25	0.509	0.935	1.945	0.491	0.306	RELAB
Howardite + CM	PRA04401	0–45	0.101	0.942	1.970	0.163	0.076	Cloutis et al. (2013)
Howardite + CM	PRA04401	45–90	0.061	0.936	1.949	0.273	0.187	Cloutis et al. (2013)
Howardite + CM	PRA04401	90–250	0.067	0.941	1.918	0.218	0.181	Cloutis et al. (2013)
Mixture	100Millbillillie + 0Murchinson	0–45	0.432	0.950	1.998	0.483	0.246	Cloutis et al. (2013)
Mixture	95Millbillillie + 5Murchinson	0–45	0.331	0.951	2.008	0.425	0.199	Cloutis et al. (2013)
Mixture	90Millbillillie + 10Murchinson	0–45	0.286	0.951	2.011	0.373	0.172	Cloutis et al. (2013)
Mixture	80Millbillillie + 20Murchinson	0–45	0.204	0.951	2.015	0.307	0.131	Cloutis et al. (2013)
Mixture	70Millbillillie + 30Murchinson	0–45	0.164	0.950	2.019	0.249	0.106	Cloutis et al. (2013)
Mixture	60Millbillillie + 40Murchinson	0–45	0.130	0.951	2.071	0.212	0.090	Cloutis et al. (2013)
Mixture	50Millbillillie + 50Murchinson	0–45	0.112	0.951	2.071	0.167	0.072	Cloutis et al. (2013)
Mixture	40Millbillillie + 60Murchinson	0–45	0.090	0.952	2.071	0.131	0.061	Cloutis et al. (2013)
Mixture	0Millbillillie + 100Murchinson	0–45	0.055	1.018	2.071	0.014	0.025	Cloutis et al. (2013)
Mixture	100PYX042 + 0MET101	0–45	0.530	0.915	1.854	0.503	0.318	Cloutis et al. (1990)
Mixture	90PYX042 + 10MET101	0–45	0.363	0.913	1.860	0.396	0.220	Cloutis et al. (1990)
Mixture	80PYX042 + 20MET101	0–45	0.267	0.912	1.859	0.323	0.166	Cloutis et al. (1990)
Mixture	70PYX042 + 30MET101	0–45	0.220	0.912	1.864	0.271	0.132	Cloutis et al. (1990)
Mixture	60PYX042 + 40MET101	0–45	0.191	0.912	1.861	0.202	0.095	Cloutis et al. (1990)
Mixture	50PYX042 + 50MET101	0–45	0.174	0.912	1.851	0.164	0.076	Cloutis et al. (1990)
Mixture	40PYX042 + 60MET101	0–45	0.177	0.913	1.859	0.169	0.083	Cloutis et al. (1990)
Mixture	30PYX042 + 70MET101	0–45	0.137	0.913	1.878	0.096	0.041	Cloutis et al. (1990)
Mixture	20PYX042 + 80MET101	0–45	0.129	0.914	1.907	0.056	0.018	Cloutis et al. (1990)
Mixture	10PYX042 + 90MET101	0–45	0.122	0.916	1.690	0.022	0.005	Cloutis et al. (1990)
Mixture	0PYX042 + 100MET101	0–45	0.111	1.390	1.690	0.000	0.000	Cloutis et al. (1990)
Mixture	100PYX042 + 0MET101	45–90	0.367	0.912	1.841	0.811	0.671	Cloutis et al. (1990)
Mixture	50PYX042 + 50MET101	45–90	0.169	0.910	1.860	0.394	0.269	Cloutis et al. (1990)
Mixture	0PYX042 + 100MET101	45–90	0.121	1.101	1.690	0.000	0.000	Cloutis et al. (1990)

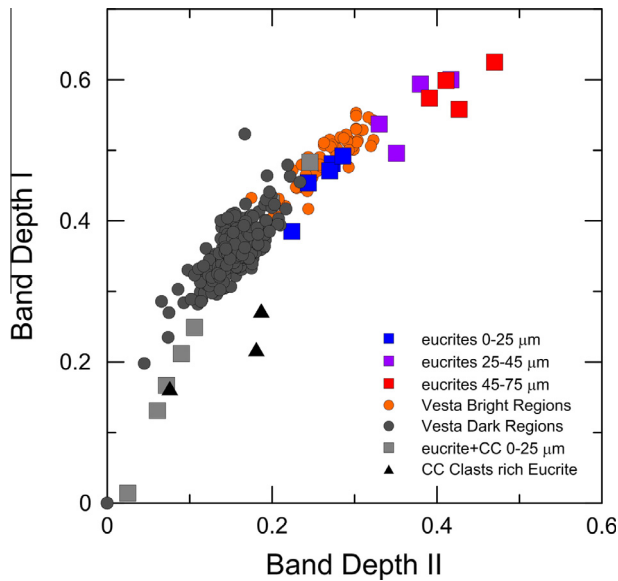


Fig. 8. Band I depth versus Band II depth scatterplot. Band I and Band II depth for all the Vesta dark material (dark gray dots) and some of the bright material (orange dots) units detected by VIR. The considered BM units are taken from Zambon et al. (2014). A lower band depth value for DM is also observed. Band depths of HED samples at different grain sizes are also plotted. The effect of the increasing grain size is to increase the band depths. (For interpretation of the references to colour in this figure legend, the reader is referred to the web version of this article.)

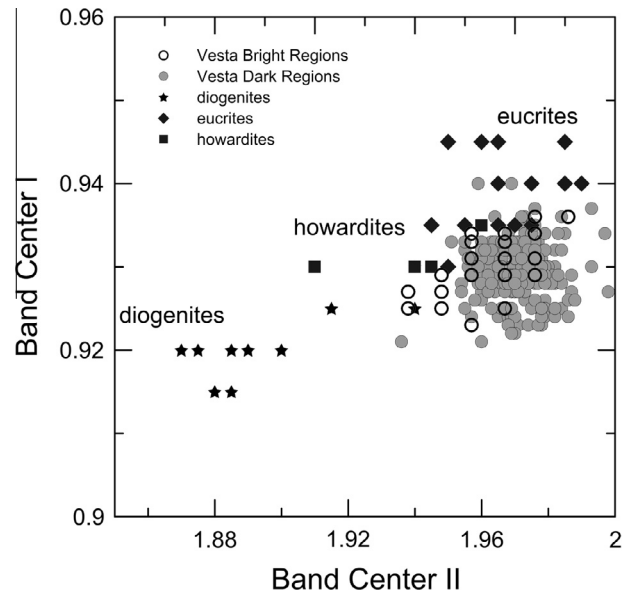


Fig. 10. Band I Center versus Band II Center scatterplot. This scatterplot helps to infer the composition of DM (gray dots) and BM units (gray diamonds). Band centers located at shorter wavelengths correspond to diogenites, whereas longer wavelengths correspond to eucrites. Most of the DM and BM have a eucritic to howarditic/eucritic composition. The eucritic component is even larger in DM units.

All the Vesta units, both bright and dark, fall in the same grain size region, confirming the previous results i.e., that the grain size is not the cause of the albedo variations across Vesta (Fig. 11b).

5.3. CC versus impact melts

The scatterplot shows a nearly linear decrease of band depth and reflectance for increasing content of CC in the eucrite–Murchison intimate mixture (see Fig. 11a and Table 2) which correlates well with the DM–BM clusters (Fig. 11b): the direction from bright towards dark materials on Vesta has the same direction of the increasing carbonaceous chondrite abundance in the mixture, suggesting a close relationship between the two dataset. However, other darkening agents cannot be excluded.

The meteorite Padarninkai is the most heavily shocked eucrite known (Yamaguchi et al., 1993); the RELAB spectra we used in our analysis are from an impact melt rich sample of Padarninkai and their position on the scatterplot is compatible with dark materials (for both the grain size intervals 0–25 and 25–45 μm). The eucrite breccia Macibini has an impact melt clast composed of approximately 50% devitrified glass and 50% silicates (Buchanan et al., 2000), located close to both Padarninkai and to the DM cluster. Thus, shock processed HED cannot be excluded as a possible dark component on Vesta, even if there are examples of other shocked HED that have high albedo properties.

Other possible darkening agents are metals, and even if the presence of large abundance of metals is unlikely, we also plot the pyroxene metal mixture group (Fig. 11a). The presence of metal in a mixture tends to lower both the albedo and the band depth II, similar to what is observed for CC–eucrite mixture: their behavior is practically coincident especially for lower amount of darkening agent (metal or CC).

The scatterplot of OH band depth versus albedo for all the VIR observations (Fig. 12) shows that band depth increases as albedo decreases, as found in De Sanctis et al. (2012b).

This strongly suggests that the most plausible explanation for low albedo material is addition of a carbonaceous chondrite-OH rich material. If we include DM units in this scatterplot, we note

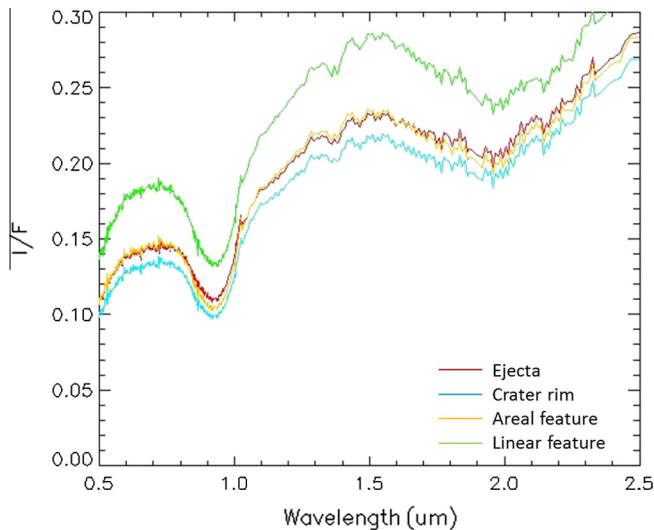


Fig. 9. DM spectra variability. Average spectra of DM of the different types. Whereas the spectra of an ejecta (VD3), crater rim (VD7) and areal feature (D54) are similar to each other, the linear feature (D83) spectrum shows an average higher reflectance and deeper band depths.

for the 0–25 μm, 25–45 μm size, by linearly fitting the points corresponding to each size interval.

It is interesting to look at the behavior of the CC-clast rich eucrite PRA 04401 at different grain sizes and the eucrite–Murchison mixture series (Fig. 11a and b): the two larger size intervals for PRA 04401 (45–90 and 90–250 μm) are nearly coincident, whereas the smaller size interval (0–45 μm) moves towards the dark mixture set, which is in the same size interval. This is further evidence that this scatterplot is very sensitive to grain size, especially for the smaller sizes.

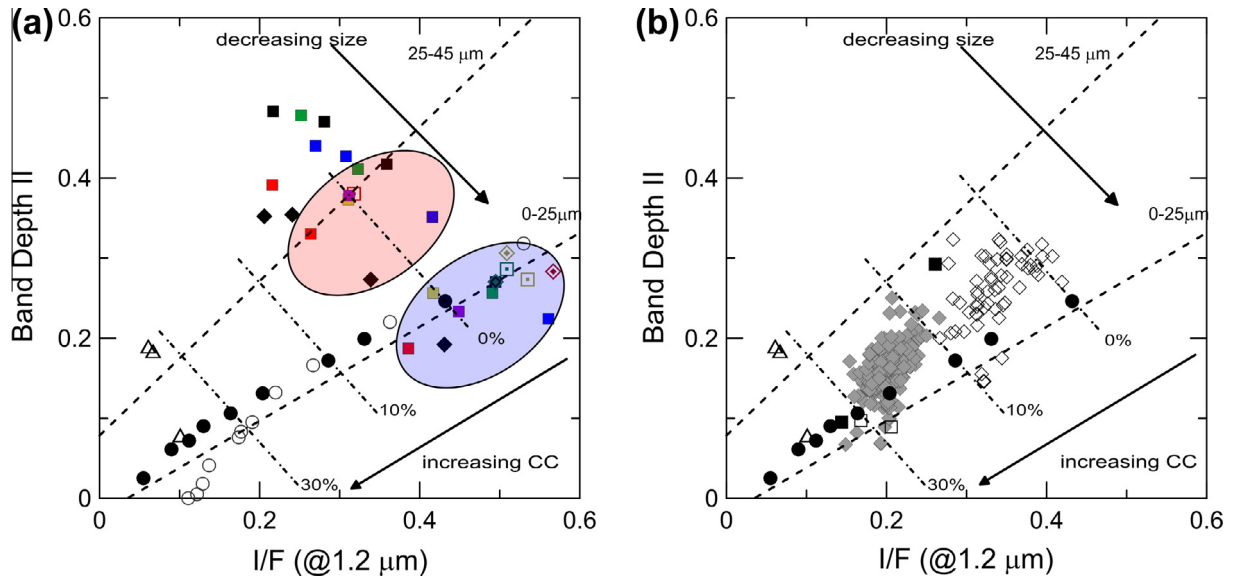


Fig. 11. Band II depth versus reflectance at 1.2 μm . (a) Eucrites (squares) and howardites (diamonds) at different grain sizes. Different colors correspond to different meteorite samples: ALHA76005 (blue square), Juvinas (black square), Y-74450 (red square), ALH78132 (green square), Padvarnikai (yellow square), Stannern (purple square), Millbillillie (open red square), Pasamonte (open green square), A-881819 (open yellow square), EET87503 (black diamond), EET83376 (open red diamond), Petersburg (open green diamond), Y-790727 (open yellow diamond). The black circles represent the intimate mixtures of a eucritic material (Millbillillie) and the Murchison CM2 meteorite at increasing abundance of the carbonaceous chondrite contaminant and with grain size of 0–25 μm (Cloutis et al., 2013). The open circles represent the mixture of pyroxene and a metal contaminant at different abundances with grain size of 0–45 μm (Cloutis et al., 1990). The open triangles are PRA04401 CC clast-rich howardite at different grain sizes. The dashed lines are the 0%, the 10% and the 30% carbonaceous chondrite abundance boundaries. The 0–25 μm and the 25–45 μm grain size clusters are encircled by light blue and pink ellipses, respectively. (b) The black circles, two arrows and dashed lines are the same as on Fig. 11a. The BM cluster (open diamonds) is located in the howardite–eucrite region (Fig. 11a) and is placed together with the DM cluster (gray diamonds) between the 25–45 μm and 0–25 μm fields. The direction BM–DM (decreasing of both reflectance and band depth) is the same as for the increasing darkening agent and the dark material units are located between 10% and 30 vol.% of CC abundance lines. The open triangles are PRA04401 CC clast-rich howardite at different grain sizes. The open and black squares are the impact melt rich samples of the Padvarnikai (0–25, 25–45 μm) and the Macibini meteorites (0–63 μm). Even shock-processed eucrites are located very close to the DM cluster border. (For interpretation of the references to colour in this figure legend, the reader is referred to the web version of this article.)

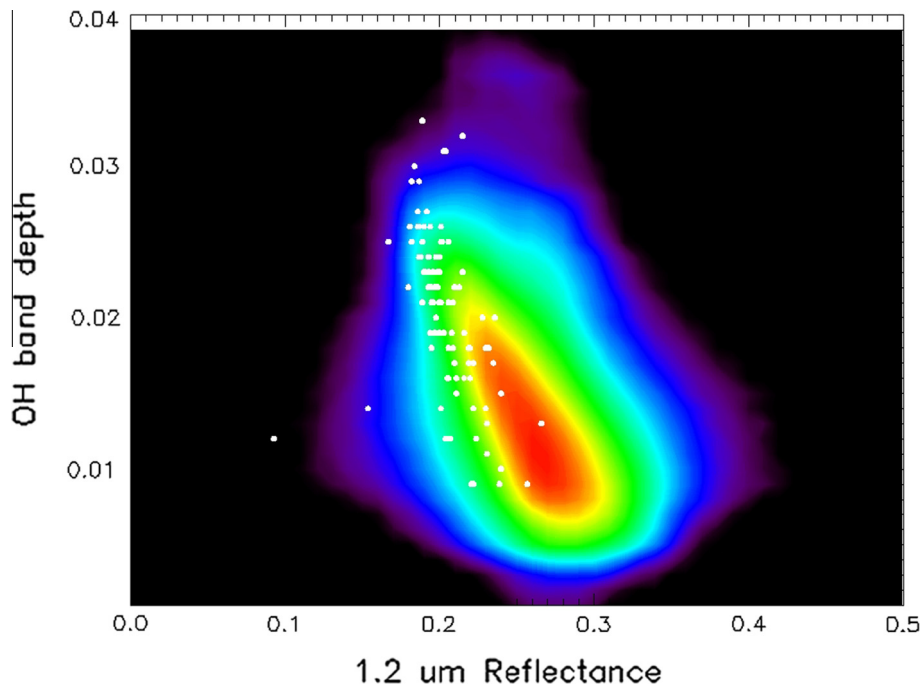


Fig. 12. OH-band depth (absolute) versus albedo @ 1.2 μm scatterplot. The white circles represent the dark material units; they are super-imposed on the density plot of the whole Vesta dataset (number of observations increases from black to red, where black indicates less than 150 observations). The DM units follow the same behavior of the whole Vesta surface, with OH-band depth increasing with decreasing albedo. Only a few points seem to depart from this behavior and are typically affected by a larger uncertainty (lower S/N ratio).

that they clearly follow this general trend (Fig. 12), confirming that even for the individual dark material units, the main source is the CC materials, with shock processed materials or metals possibly present as minor products since they are not expected to have stronger 2.8 μm band depths. This does not exclude that, rarely, shock processed materials and metals can be present as a major source but only in a few individual units.

A cross check with the DM catalogue (Table 1) confirms that more than 90% of the dark material units show an OH absorption band depth between 1% and 3.3%, whereas for less than 10%, the OH absorption feature seems to be absent or very weak. In Fig. 13 we show an example of two units, the dark ejecta VD3 and the linear feature D83. Interestingly the D83 does not follow the typical trend of OH band depth versus albedo seen on Vesta. In one observation, the OH feature was not detected, whereas in the other observation (shown in Fig. 13), the very weak OH absorption band is completely independent from the albedo. Therefore, unit D83 could be one rare example of dark material not containing carbonaceous chondrite.

5.4. CC abundance and grain size evaluation on Vesta

By using the reflectance versus BDII scatterplot (Fig. 11a and b), we can try to evaluate both the grain size and the CC abundance in dark material units.

As far as the grain size is concerned, both the dark and the bright material units have on average the same size. With only very few exceptions, the Vestan dark and bright materials lie between the 0–25 and 25–45 μm size boundaries. From this result it is evident that, on Vesta, the regolith grain size seems to be nearly constant with an average value of 25 μm , and a maximum value of 45 μm . This could have important consequences on the surface evolutionary scenarios, as opposed to the current view where the brightest material is the most pristine and can possibly be associated with coarse grained or coherent rocks whereas the darkest units are the more processed and mixed and could have undergone efficient comminution, reducing their size (e.g. Li et al., 2013).

The same scatterplot shows a nearly linear decrease of band depth and reflectance for increasing content of CC in the

euclite–Murchison intimate mixture (see Fig. 11a and Table 2). If we take that linear trend as reference, the retrieved abundance of the CC component in PRA 04401 should be about 50%, similar to the value ($\sim 40\%$ of visible CM2 clasts) estimated by Cloutis et al. (2013). Moreover it is useful to remark that the total modal abundance of visible carbonaceous chondrite fragments in the PRA 04401 meteorite is $\sim 60\%$ (Herrin et al., 2011). This implies that the reflectance-BDII scatterplot can be a reliable method to evaluate the CC abundance in a mixture with euclites and that we can define the boundaries for different CC abundance (as an example in Fig. 11a and b we plotted the 0%, the 10% and the 30% lines).

By assuming such a fine regolith size, using the euclite–Murchison intimate mixtures (at 0–45 μm) is a proper way to evaluate the abundance of carbonaceous chondrite material in DM units.

Again, on the same scatterplot (Fig. 11b), nearly all the DM units on Vesta are located within the boundaries of 10–30 vol.% of CC. This global result does not exclude that on a local scale, single units may show larger abundance of carbonaceous material. However, it is important to remark that among all the DM units we were not able to find a single unit composed of a pure carbonaceous chondrite. Extrapolating this result to the bright units, it appears that many of them are still contaminated by smaller amounts ($<10\%$) of carbonaceous chondrite material and that it is very difficult to find bright materials completely free of dark contaminant.

6. Conclusions

In this work, dark material units have been detected and then defined on the surface of Vesta. We defined DM units assuming a relative reflectance criterion, i.e., areas showing a reflectance lower than the surroundings. By coupling visible and infrared images of the same area, we are able to select real dark material units, discarding illumination effects, such as shadowed or poorly illuminated regions that are also typically cold. We compiled a detailed DM catalogue that includes 104 dark units (i.e. reflectance at least 15% lower than the surroundings) and 19 very dark units (i.e., reflectance at least 30% lower than the surroundings). Most (60%) of the DM units are associated with impact-related features, i.e., ejecta or craters (rim, floor or wall). Other DM units are associated with areal features and linear features. As found by Jaumann et al. (2014) by using Framing Camera data, we confirm a larger concentration of DM units around the Veneneia impact basin.

The spectral properties of the DM have been discussed by applying a photometric correction of the parameters such as band depth, band center, BAR, and OH band depth. The parameters which best characterize DM, besides reflectance, are the depths of Band I and Band II, which are always lower than the Vesta average and the bright units. Conversely, band centers and BAR do not change, suggesting a composition similar to the average Vesta surface. The only relevant compositional difference is that the darker materials seem to be slightly more euclitic than the bright ones. In contrast to what was inferred by Reddy et al. (2012c), even a detailed study of the albedo versus BDII does not allow one to determine the origin of DM units, because both the impact melt and the euclite–CC mixture can be plausible sources. A definitive element in favor of a carbonaceous chondritic origin for most of the DM is given by the OH absorption band depth versus reflectance scatterplot behavior, where the darkest DM are also the richest in OH, similarly to what was found by De Sanctis et al. (2012b). In this scenario, shock processed materials may be present in a few areas as minor products. One example of this type seems to be represented by the linear feature D83, which is an OH-free DM deposit. There are few possible explanations for the presence of DM units not enriched in OH. One possibility is that they include CC material dehydrated by violent impacts (see, e.g.

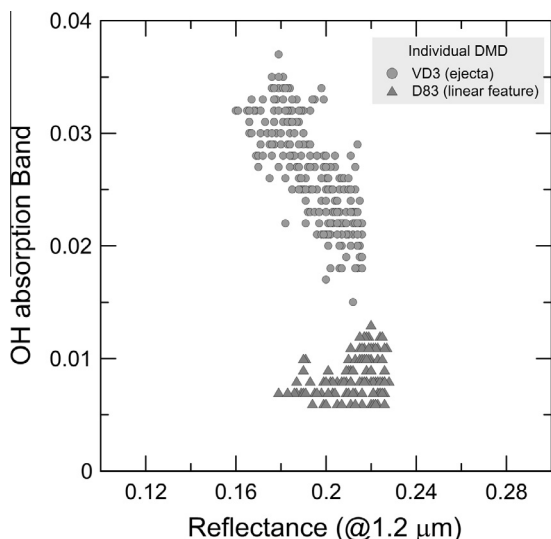


Fig. 13. OH-band depth versus albedo @ 1.2 μm scatterplot. Behavior of two individual observations of two different dark units taken from the catalogue (VD3 and D83). The D83 unit shows a very weak OH band depth that is independent of albedo.

Rubin and Bottke, 2009), and this fits well with the fact that this kind of impact should be marginal with respect to the average low velocity impacts which hit Vesta. Another possibility is that they are impact melts, and even this scenario fits well with the scarcity of observed melts among the HED meteorites (McSween et al., 2013) or on Vesta (Schenk et al., 2012). A third very interesting possibility is they are anhydrous metal rich materials. Meteorites of this type include mesosiderites, which could contain up to 50% metal (Scott et al., 2014) and were recently proposed to have originated from Vesta (Greenwood et al., 2006; Scott et al., 2014), even if the first attempts to detect them by means of the VIR spectra failed (Palomba et al., 2012). A follow-up in-depth analysis of these “dry” DM units is planned in the near future to better clarify their nature.

Finally, we have shown that the BDII versus reflectance scatterplot can be used to infer carbonaceous chondrite abundance and grain size of the uppermost regolith of Vesta. According to laboratory data, the maximum retrieved abundance of dark contaminant is less than 30 vol.% of carbonaceous chondrites, a value well below the typical value found for PRA04401 (60%), while the grain size on Vesta is possibly around an average value of 25 μm , and seems to be not much larger than 45 μm . Geological analysis demonstrates that the dark material is concentrated in the first 2 km of the sub-surface as isolated patches and that impact excavation is the more important mechanism to bring both fresh brighter material and dark patches to the surface or near the surface (Jaumann et al., 2014). The apparent size homogeneity we observe among all the materials on the surface of Vesta indicates that the regolith grain size should be well mixed horizontally and vertically, at least in the first hundreds of meters beneath the surface. The fact that thick patches of DM are found at depth and have the same fine grain size of all the other DM units, suggests that the collisional erosion should have been a marginal process. It is more likely that the present DM size is close to the original accreted size. If true, this result would argue against the scenario of large blocks of spall material from impacts with carbonaceous asteroids at the origin of the DM units (Reddy et al., 2012b; McCord et al., 2012), or a continuous flux of meteoroids (Turrini et al., 2014) and would support the idea that DM was accreted in the form of dust (De Sanctis et al., 2012b). The burial further constrains the accretion to be older than the Rheasilvia basin-forming event (the last major event that may have generated a thick layer of regolith) but not necessarily older than the Veneneia basin-forming event. A model of regolith redistribution due to the major observed craters (Marchi et al., 2012) is needed in order to see if this scenario is consistent with the spatial distribution of the DM units.

Acknowledgments

VIR is funded by the Italian Space Agency-ASI and was developed under the leadership of INAF-Istituto di Astrofisica e Planetologia Spaziali, Rome-Italy. The instrument was built by Selex-Galileo, Florence-Italy. The authors acknowledge the support of the Dawn Science, Instrument, and Operations Teams. This work was supported by ASI-Italy and NASA-United States. A portion of this work was performed at the NASA/JPL. We warmly thank Sharon Uy (UCLA) for manuscript revisions, Vishnu Reddy (PSI) for ample discussions about spectral parameters, S. Marchi for fruitful discussions about the DM origin scenarios, Paul C. Buchanan, Tasha Dunn and an anonymous reviewer for thorough and very constructive reviews which helped to improve our manuscript. The data used in this paper are available from the website <http://dawndata.igpp.ucla.edu>.

References

- Adams, J.B., Filice, A.L., 1967. Spectral reflectance 0.4 to 2.0 μm of silicate rock powders. *J. Geophys. Res.* 72, 5705–5715.
- Adams, J.B., Horz, F., Gibbons, R.V., 1979. Effects of shock-loading on the reflectance spectra of plagioclase, pyroxene, and glass. *Lunar Planet. Sci.* 10, 1–3.
- Ammannito, E. et al., 2013a. Vestan lithologies mapped by the visual and infrared spectrometer. *Meteorit. Planet. Sci.* <http://dx.doi.org/10.1111/maps.12192>.
- Ammannito, E. et al., 2013b. Olivine in an unexpected location on Vesta's surface. *Nature*. <http://dx.doi.org/10.1038/nature12665>.
- Beck, J.B., Barrat, J.-A., Grisolle, F., Quirico, E., Schmitt, B., Moynier, F., Gillet, P., Beck, C., 2011. NIR spectral trends of HED meteorites: Can we discriminate between the magmatic evolution, mechanical mixing and observation geometry effects? *Icarus* 216, 560–571.
- Binzel, R.P., Gaffey, M.J., Thomas, P.C., Zellner, B.H., Storrs, A.D., Wells, E.N., 1997. Geologic mapping of Vesta from 1994 Hubble Space Telescope images. *Icarus* 128 (1), 95–103.
- Britt, D.T., Pieters, C.M., 1994. Darkening in black and gas-rich ordinary chondrites: The spectral effects of opaque morphology and distribution. *Geochim. Cosmochim. Acta* 58 (18), 3905–3919.
- Buchanan, P.C., Lindstrom, D.J., Mittlefehldt, D.W., Koeberl, C., Reimold, W.U., 2000. The South African polymict eucrite Macibini. *Meteorit. Planet. Sci.* 35, 1321–1331.
- Burbine, T.H. et al., 2001. Vesta, Vestoids, and the howardite, eucrite, diogenite group: Relationships and the origin of spectral differences. *Meteorit. Planet. Sci.* 36, 761–781.
- Burbine, T.H., Buchanan, P.C., Dolkar, T., Binzel, R.P., 2009. Pyroxene mineralogies of near-Earth vestoids. *Meteorit. Planet. Sci.* 44 (9), 1331–1341.
- Clark, R.N., Roush, T.L., 1984. Reflectance spectroscopy – Quantitative analysis techniques for remote sensing applications. *J. Geophys. Res.* 89, 6329–6340.
- Clark, B.E., Fanale, F.P., Salisbury, J., 1992. Meteorite–asteroid spectral comparison: The effects of comminution, melting and recrystallization. *Icarus* 97, 288–297.
- Clemett, S.J., Nakamura-Messenger, K., Thomas-Keprta, K.L., Messenger, S., McKay, D.S., 2010. The spatial distribution and mineralogical association or organics in the Tagish Lake and Bells carbonaceous chondrites. *Lunar Planet. Sci.* 2347.
- Cloutis, E.A., Gaffey, M.J., 1991. Spectral–compositional variations in the constituent minerals of mafic and ultramafic assemblages and remote sensing implications. *Earth, Moon, Planets* 53, 11–53.
- Cloutis, E.A., Gaffey, M.J., Jackowski, T.L., Reed, K.L., 1986. Calibrations of phase abundance, composition, and particle size distribution for Olivine–Orthopyroxene mixtures from reflectance spectra. *J. Geophys. Res.* 91 (B11), 11641–11653.
- Cloutis, E.A., Gaffey, M.J., Smith, D.G.W., Lambert, R.St.J., 1990. Metal silicate mixtures: Spectral properties and applications to asteroid taxonomy. *J. Geophys. Res.* 95, 8323–8338.
- Cloutis, E.A., Izawa, M.R.M., Pompilio, L., Reddy, V., Hiesinger, H., Nathues, A., Mann, P., Le Corre, L., Palomba, E., Bell III, J.F., 2013. Spectral reflectance properties of HED meteorites + CM2 carbonaceous chondrites: Comparison to HED grain size and compositional variations and implications for the nature of low-albedo features on Asteroid 4 Vesta. *Icarus* 223, 850–877.
- Coradini, A. et al., 2011. The surface composition and temperature of Asteroid 21 Lutetia as observed by Rosetta/VIRTIS. *Science* 334 (6055), 492–494.
- De Sanctis, M.C. et al., 2011. The VIR spectrometer. *Space Sci. Rev.* 163, 329–369.
- De Sanctis, M.C. et al., 2012a. Spectroscopic characterization of mineralogy and its diversity across Vesta. *Science* 336 (6082), 697–700.
- De Sanctis, M.C. et al., 2012b. Detection of widespread hydrated materials on Vesta by the VIR imaging spectrometer on board the Dawn mission. *Astrophys. Lett.* 758 (2), L36, 5pp. <http://dx.doi.org/10.1088/2041-8205/758/2/L36>.
- De Sanctis, M.C. et al., 2013. Vesta's mineralogical composition as revealed by VIR on Dawn. *Meteorit. Planet. Sci.* <http://dx.doi.org/10.1111/maps.12138>.
- Denevi, B.W. et al., 2012. Pitted terrain on Vesta and implications for the presence of volatiles. *Science* 338 (6104), 246–249.
- Duffard, R., Lazzaro, D., de León, J., 2005. Revisiting spectral parameters of silicate bearing meteorites. *Meteorit. Planet. Sci.* 40, 445–459.
- Gaffey, M.J., 1976. Spectral reflectance characteristics of the meteorite classes. *J. Geophys. Res.* 81, 905–920.
- Gaffey, M.J., 1997. Surface lithologic heterogeneity of Asteroid 4 Vesta. *Icarus* 127, 130–157.
- Gaffey, M.J., Cloutis, E.A., Kelley, M.S., Reed, K.L., 2002. Mineralogy of asteroids. In: *Asteroids III*. University of Arizona Press, Tucson, pp. 183–204.
- Garvie, L.A.J., Buseck, P.R., 2004. Nanoglobules, macromolecular materials, and carbon sulfides in carbonaceous chondrites. *Lunar Planet. Sci.* 1789.
- Greenwood, R.C., Franchi, I.A., Jambon, A., Barrat, J.A., Burbine, T.H., 2006. Oxygen isotope variation in stony-iron meteorites. *Science* 313, 1763–1765.
- Herrin, J.S., Zolensky, R.E., Cartwright, J.A., Mittlefehldt, D.W., Ross, D.K., 2011. Carbonaceous chondrite-rich howardites: the potential for hydrous lithologies on the HED parent. *Lunar Planet. Sci.* 42, 2806.
- Hiroi, T., Binzel, R.P., Sunshine, J.M., Pieters, C.M., Takeda, H., 1995. Grain sizes and mineral compositions of surface regoliths of Vesta-like asteroids. *Icarus* 115, 374–386.
- Irving, A.J., 2012. Constraints on the Mineralogy of Mantle Source Regions of Primary Shergottite Magmas. The Mantle of Mars: Insights from Theory, Geophysics, High-Pressure Studies, and Meteorites, September 10–12, Houston, Texas. LPI Contribution No. 1684, id. 13.

- Jaumann, R. et al., 2012. Vesta's shape and morphology. *Science* 336 (6082), 687–690.
- Jaumann, R., Nass, A., Otto, K., Krohn, K., McCord, T.B., Williams, D.A., Raymond, C.A., Stephan, K., Blewett, D.T., Hiesinger, H., Yingst, R.A., De Sanctis, M.C., Palomba, E., Roatsch, T., Matz, K.-D., Russell, C.T., 2014. The geological nature of dark material on Vesta and implications for the subsurface structure. *Icarus* 240, 3–19.
- Johnson, J.R., Horz, F., 2003. Visible/near-infrared spectra of experimentally shocked plagioclase feldspars. *J. Geophys. Res.* 108 (E11), 6–1. <http://dx.doi.org/10.1029/2003JE002127> (CiteID 5120).
- Kebukawa, Y. et al., 2010. Spatial distribution of organic matter in the Bells CM2 chondrite using near-field infrared microspectroscopy. *Meteorit. Planet. Sci.* 45, 394–405.
- Keilm, S., Tosi, F., Kamp, L., Capaccioni, F., Gulik, S., Grassi, D., Hofstadter, M., Filacchione, G., Lee, S., Giuppi, S., Janssen, M., Capria, M., 2012. Interpretation of combined infrared, submillimeter, and millimeter thermal flux data obtained during the Rosetta fly-by of Asteroid (21) Lutetia. *Icarus* 221 (1), 395–404.
- Li, J.-Y., McFadden, L.A., Thomas, P.C., Mutchler, M.J., Parker, J.W., Young, E.F., Russell, C.T., Sykes, M.V., Schmidt, B.E., 2010. Photometric mapping of Asteroid (4) Vesta's southern hemisphere with Hubble Space Telescope. *Icarus* 208 (1), 238–251.
- Li, J.-Y., Le Corre, L., Schröder, S.E., Reddy, V., Buratti, B.J., Mottola, S., Hoffmann, M., Nathues, A., Russell, C.T., Raymond, C.A., 2013. Global photometric properties of Asteroid (4) Vesta observed with Dawn Framing Camera. *Icarus* 226 (2), 1252–1274.
- Li, Jian-Yang, Mittlefehldt, D.W., Pieters, C.M., De Sanctis, M.C., Schröder, S.E., Hiesinger, H., Williams, D.A., Beck, A.W., Ammannito, E., Capaccioni, F., Capria, M.T., Palomba, E., Carsenty, U., Keller, U., Russell, C.T., Raymond, C.A., Jaumann, R., McSween, H.Y., McCord, T.B., Denevi, B.W., Sunshine, J.M., 2014. Vesta's bright, primordial material. *Icarus* (submitted for publication).
- Longobardo, A., Palomba, E., Capaccioni, F., De Sanctis, M.C., Tosi, F., Ammannito, E., Schröder, S.E., Zambon, F., Raymond, C.A., Russell, C.T., 2014. Photometric behavior of spectral parameters in Vesta dark and bright regions as inferred by the Dawn VIR spectrometer. *Icarus* 240, 20–35.
- Mason, B., 1962. The carbonaceous chondrites. *Space Sci. Rev.* 1, 621–646.
- Mayne, R.G., Sunshine, J.M., McSween, H.Y., McCoy, T.J., Corrigan, C.M., Gale, A., 2010. Petrologic insights from the spectra of the unbrecciated eucrites: Implications for Vesta and basaltic asteroids. *Meteorit. Planet. Sci.* 45 (7), 1074–1092.
- McCord, T.B., Adams, J.B., Johnson, T.V., 1970. Asteroid Vesta: Spectral reflectivity and compositional implications. *Science* 168 (3938), 1445–1447.
- McCord, T.B. et al., 2012. Dark material on Vesta from the infall of carbonaceous volatile-rich material. *Nature* 7422 (491), 83–86. <http://dx.doi.org/10.1038/nature11561>.
- McSween, H.Y., Mittlefehldt, D.W., Beck, A.W., Mayne, R.G., McCoy, T.J., 2011. HED meteorites and their relationship to the geology of Vesta and the Dawn mission. *Space Sci. Rev.* 163 (1–4), 141–174.
- McSween, H.Y. et al., 2013. Dawn, the Vesta – HED connection, and the geologic context for eucrites, diogenites, and howardites. *Meteorit. Planet. Sci.* <http://dx.doi.org/10.1111/maps.12108>.
- Moskovitz, N.A., Willman, M., Burbine, T.H., Binzel, R.P., Bus, S.J., 2010. A spectroscopic comparison of HED meteorites and V-type asteroids in the inner main belt. *Icarus* 208, 773–788.
- Palomba, E. et al., 2012. Composition and mineralogy of dark material deposits on Vesta, 43rd Lunar and Planetary Science Conference, March 19–23, The Woodlands, Texas. LPI Contribution No. 1659, id. 1930.
- Palomba, E. et al., 2013. Mesosiderite on Vesta: A hyperspectral Vis–NIR investigation. *Lunar Planet. Sci.* 44, 2245.
- Pearson, V.K., Sephton, M.A., Kearsley, A.T., Bland, P.A., Franchi, I.A., Gilmour, I., 2002. Clay mineral–organic matter relationships in the early Solar System. *Meteorit. Planet. Sci.* 37, 1829–1833.
- Prettyman, T.H. et al., 2011. Dawn's gamma ray and neutron detector. *Space Sci. Rev.* 163, 371–459.
- Prettyman, T.H. et al., 2012. Elemental mapping by Dawn reveals exogenic H in Vesta's regolith. *Science* 338 (6104), 242–246.
- Reddy, V. et al., 2012a. Color and albedo heterogeneity of Vesta from Dawn. *Science* 336 (6082), 700–704.
- Reddy, V., Le Corre, L., O'Brien, D.P., Nathues, A., Cloutis, E.A., Durda, D.D., Bottke, W.F., Bhatt, M.U., Nesvorniy, D., Buczkowski, D., Scully, J.E.C., Palmer, E.M., Sierks, H., Mann, P.J., Becker, K.J., Beck, A.W., Mittlefehldt, D., Li, J.-Y., Gaskell, R., Russell, C.T., Gaffey, M.J., McSween, H.Y., McCord, T.B., Combe, J.-P., Blewett, D., 2012b. Delivery of dark material to Vesta via carbonaceous chondritic impacts. *Icarus* 221 (2), 544–559.
- Reddy, V., Sanchez, J.A., Nathues, A., Moskovitz, N.A., Li, J.-Y., Cloutis, E.A., Archer, K., Tucker, R.A., Gaffey, M.J., Paul Mann, J., Sierks, H., Schade, U., 2012c. Photometric, spectral phase and temperature effects on 4 Vesta and HED meteorites: Implications for the Dawn mission. *Icarus* 217, 153–158.
- Rubin, A.E., Bottke, W.F., 2009. On the origin of shocked and unshocked CM clasts in H-chondrite regolith breccias. *Meteorit. Planet. Sci.* 44 (5), 701–724.
- Ruff, S.W., Christensen, P.R., 2002. Bright and dark regions on Mars: Particle size and mineralogical characteristics based on Thermal Emission Spectrometer data. *J. Geophys. Res.* 107 (E12), 2–1–2–22.
- Russell, C.T. et al., 2007. Exploring the asteroid belt with ion propulsion: Dawn mission history, status and plans. *Adv. Space Res.* 40 (2), 193–201.
- Russell, C.T. et al., 2012. Dawn at Vesta: Testing the protoplanetary paradigm. *Science* 336 (6082), 684–686.
- Schenk, P. et al., 2012. The geologically recent giant impact basins at Vesta's south pole. *Science* 336, 694–697. <http://dx.doi.org/10.1126/science.1223272>.
- Schroder, S.E., Mottola, S., Keller, H.U., Raymond, C.A., Russell, C.T., 2013. Resolved photometry of Vesta reveals physical properties of crater regolith. *Planet. Space Sci.* (in press). doi: <http://dx.doi.org/10.1016/j.pss.2013.06.009>.
- Scott, E.R.D., Bottke, W.F., Marchi, S., Delaney, J.S., 2014. How did mesosiderites form and do they come from Vesta or a Vesta-like body? *Lunar Planet. Sci.* 45, 2260.
- Shkuratov, Y.G., Kreslavsky, M.A., Ovcharenko, A.A., Stankevich, D.G., Zubko, E.S., Pieters, C., Arnold, G., 1999. Opposition effect from Clementine data and mechanisms of backscatter. *Icarus* 141, 132–155.
- Sierks, H. et al., 2011. The Dawn framing camera. *Space Sci. Rev.* 163, 263–327.
- Tosi, F., Capria, M.T., De Sanctis, M.C., Combe, J.-Ph., Zambon, F., Nathues, A., Schröder, S.E., Li, J.-Y., Palomba, E., Longobardo, A., Blewett, D.T., Denevi, B.W., Palmer, E., Capaccioni, F., Sunshine, J.M., Ammannito, E., Titus, T., Mittlefehldt, D.W., Russell, C.T., Raymond, C.A., and the Dawn/VIR Team, 2014. Thermal measurements of dark and bright surface features on Vesta as derived from Dawn/VIR. *Icarus* 240, 36–57.
- Turrini, D., Combe, J.-P., McCord, T.B., Okay, N., Vincent, J.-B., Prettmann, T.H., McSween, H.Y., Consolmagno, G.J., De Sanctis, M.C., Le Corre, L., Longobardo, A., Palomba, E., Russell, C.T., 2014. The contamination of the surface of Vesta by impacts and the delivery of the dark material. *Icarus* 240, 86–102.
- Yamaguchi, A., Mori, H., Takeda, H., 1993. Mineralogy and shock textures in the Padarninkai eucrite (abstract). *Meteoritics* 28, 462–463.
- Zambon, F., De Sanctis, M.C., Schröder, S.E., Tosi, F., Li, J.-Y., Longobardo, A., Ammannito, E., Blewett, D.T., Palomba, E., Capaccioni, F., Frigeri, A., Mittlefehldt, D.W., Nathues, A., Pieters, C., Russell, C.T., Raymond, C.A., 2014. Spectral analysis of the bright materials on the asteroid Vesta. *Icarus* 240, 73–85.
- Zolensky, M.E., Weisberg, M.K., Buchanan, P.C., Mittlefehldt, D.W., 1996. Mineralogy of carbonaceous chondrite clasts in HED achondrites and the Moon. *Meteorit. Planet. Sci.* 31 (4), 518–537.